NEUTRON SPECTROSCOPY OPTIMIZATION USING A SOLID STATE THERMAL NEUTRON DETECTOR

THESIS

Carl J. Eichert, 2d Lieutenant, USAF

AFIT-ENP-MS-16-M-066

DEPARTMENT OF THE AIR FORCE
AIR UNIVERSITY

AIR FORCE INSTITUTE OF TECHNOLOGY

Wright-Patterson Air Force Base, Ohio

DISTRIBUTION STATEMENT A
APPROVED FOR PUBLIC RELEASE; DISTRIBUTION UNLIMITED

The views expressed in this document are those of the author and do not reflect the official policy or position of the United States Air Force, the United States Department of Defense or the United States Government. This material is declared a work of the U.S. Government and is not subject to copyright protection in the United States.

AFIT-ENP-MS-16-M-066

NEUTRON SPECTROSCOPY OPTIMIZATION USING A SOLID STATE THERMAL NEUTRON DETECTOR

THESIS

Presented to the Faculty

Department of Engineering Physics

Graduate School of Engineering and Management

Air Force Institute of Technology

Air University

Air Education and Training Command

in Partial Fulfillment of the Requirements for the

Degree of Master of Science

Carl J. Eichert, BS

2d Lieutenant, USAF

March 2016

DISTRIBUTION STATEMENT A
APPROVED FOR PUBLIC RELEASE; DISTRIBUTION UNLIMITED

AFIT-ENP-MS-16-M-066

NEUTRON SPECTROSCOPY OPTIMIZATION USING A SOLID STATE THERMAL NEUTRON DETECTOR

THESIS

Carl J. Eichert, BS
2d Lieutenant, USAF

Committee Membership:

Dr. James C. Petrosky,
Chair

Dr. Justin A. Clinton
Member

Dr. Matthew R. Halstead
Member

AFIT-ENP-MS-16-M-066

Abstract

AFIT is researching methods for radiation detection that allow for fast analysis of neutron spectra for energies up to 14 MeV. The initial research includes the design and analysis of a neutron spectrometer using high-efficiency solid state detectors separated by multiple layers of high density polyethylene and cadmium. The spectrometer design was modeled and optimized computationally using GEANT4.10.1; a range of monoenergetic neutron sources were modeled, resulting in a theoretical response function matrix for several different polyethylene layer thicknesses. These response functions and source spectra from historical experimental data and spectra can then be used in a Maximum-Likelihood Expectation-Maximization unfolding routine to unfold the spectra of polyenergetic sources. The key to the success of this research is obtaining the resolution needed between the detectors to unfold the spectrum, while making the system of thermalizing polyethylene layers and detectors as efficient as possible. This presentation will discuss the process used to develop the algorithm and models and determine efficiency, including experiments to validate the results.

I dedicate this work to all of the people and events that have left me sad, happy, frustrated, and spirited. This hasn't been easy but it's been worth it. Thank you.

Acknowledgements

I would like to acknowledge my advisor and committee for pushing me through this challenge because it has been one of the most difficult ordeals in my life. God bless the Chuckleheads and their goofy selves. Lastly, my family and the challenges we faced together growing up have given me great strength to be the military officer that I'm becoming.

Carl J. Eichert

Table of Contents

Page

Abstract iv

Acknowledgements vi

List of Figures ix

List of Tables xii

1. Introduction 1

1.1 Overview 1
1.2 Motivation 2
Reactor Facilities and Accelerators 2
1.3 Objectives of this Research 5
1.4 Sponsor and Organization of the Thesis 6

2. Theory 7

2.1 Neutron Detection 7
Fast Neutron Detection 7
Thermal Neutron Detection 8
Semiconductor Physics 11
2.2 Neutron Moderation 17
Scattering and Moderation 18
Moderation in a Material Medium 23

3. Methodology 25

3.1 Maximum-Likelihood Expectation-Maximization Unfolding 26
General Reconstructive Iterative Methods 26
MLEM Reconstruction 27
3.2 Monte Carlo Method 29
Random Variables 30
Probability Density Function 31
Cumulative Density Function 32
Mean, Variance, and Standard Deviation 35
Sampling and Scoring 36
3.3 Geant Monte Carlo Particle Transport 42
3.4 Response Function Optimization Approach 43
PuBe Neutron Source and Initial Guess 46
Spectrum Unfolding Algorithm, Convergence, and Example Result 48

Page

3.5 Experiment . . . 52
Equipment . . . 53
Charge Carrier Detection . . . 60
Special Considerations . . . 60

4. Results and Analysis . . . 63

4.1 Response Function . . . 63
Detection Efficiency . . . 65
Source Data . . . 67
4.2 MLEM . . . 67
MLEM Proof . . . 68
4.3 Final Solutions . . . 77

5. Conclusions . . . 81

5.1 Summary . . . 81
5.2 Future Work . . . 82

Appendix A. First Appendix . . . 84

A.1 Response Functions. . . . 84
Bibliography . . . 91

List of Figures

Figure		Page
1.	Watt Spectrum.	4
2.	Fusion intensities.	5
3.	Solid state neutron detection trench design.	10
4.	Recombination.	13
5.	Generation.	14
6.	Forward and reverse biases.	16
7.	Mean free path vs neutron energy.	21
8.	Carbon microscopic cross section.	22
9.	Moderating elements and mean free paths.	23
10.	Reconstruction process for the general iterative reconstruction.	27
11.	Reconstruction process for the MLEM iterative reconstruction.	28
12.	PDF for a general exponential attenuation problem.	34
13.	CDF for a general exponential attenuation problem.	34
14.	Rejection method examples of applications: high and low probability events.	38
15.	Rejection method examples of applications: low deviation.	39
16.	Geant simulation of neutron irradiation into the spectrometer.	44
17.	Example of a well-resolved response function.	45
18.	Specific PuBe source spectrum the MLEM method used.	46
19.	Polyenergetic PuBe spectrum through the [1111111111] thickness combination (numbers by centimeter)	47

Figure Page

20. Example non-normalized linear MLEM unfolded solution with the circular point that indicates the final unfolded solution; intensity sums were equivalent to the termination point at every iteration thereafter. 50

21. Example non-normalized semilog MLEM unfolded solution with the circular point that indicates the final unfolded solution; intensity sums were equivalent to the termination point at every iteration thereafter. 51

22. Spectrometer setup with power supply and preamplifier. 52

23. Electronic configuration for the spectrometer experiment. 55

24. Electronic configuration for the spectrometer experiment. 57

25. Function generator and Oscilloscope 58

26. GammaVision interface. 59

27. Carrier current with respect to time with two charge carriers. The carrier mobility leads to different accumulated currents (top), which affects the arrival times (bottom). 61

28. Comparison of moderating characteristics of polyethylene and neutron shield concrete. 62

29. Number of neutrons detected per detector layer 64

30. Total fraction detected vs. monoenergetic neutron source count 65

31. Fraction detected per detection layer vs. monoenergetic neutron source count 66

32. Linear plot of the converging iterative MLEM solution. 69

33. Semilog plot of the converging iterative MLEM solution. 69

34. MLEM unfolded solution of a 1.0 cm thickness combination produced by the Geant model and the experiment. 77

35. Variance between the difference ratio and unity between Geant and the experiment. 78

Figure Page

36. PuBe reference source. 79

37. PuBe reference source. 80

38. HDPe thickness combination [5.0, 3.0, 5.0, 7.0, 7.0, 2.0, 2.0, 2.0, 2.0, 2.0]. 84

39. HDPe thickness combination [3.0, 2.0, 5.0, 4.0, 5.5, 2.0, 2.0, 2.0, 2.0, 2.0]. 85

40. HDPe thickness combination [3.0, 3.0, 3.5, 5.0, 5.0, 2.0, 2.0, 2.0, 2.0, 2.0]. 86

41. HDPe thickness combination [5.5, 4.0, 4.0, 5.0, 7.0, 2.0, 2.0, 2.0, 2.0, 2.0]. 87

42. HDPe thickness combination [3.3, 4.0, 3.0, 2.0, 2.0, 1.5, 2.0, 2.0, 5.0, 1.0]. 88

43. HDPe thickness combination [3.3, 4.0, 3.0, 7.5, 9.0, 2.0, 2.0, 2.0, 2.0, 2.0]. 89

44. HDPe thickness combination [1.7, 1.0, 1.0, 1.0, 1.0, 1.2, 1.5, 1.8, 1.8, 1.0]. 90

List of Tables

Table		Page
1.	Scattering microscropic cross sections at thermal and D-D reaction neutron energies.	19
2.	Several values for neutron energies and their mean free paths.	21
3.	Number of collisions to reach a specific energy from 2.45 MeV.	24
4.	Example response function data	45
5.	Example MLEM first ten iterations	49
6.	Example MLEM final iteration	50
7.	Lab Equipment Used in the Present Research	54
8.	Detection efficiency per monoenergetic neutron per detector.	67
9.	0.5 MeV MLEM	71
10.	3.0 MeV MLEM	72
11.	7.0 MeV MLEM	73
12.	9.0 MeV MLEM	74
13.	11.0 MeV MLEM	75
14.	Ratio of Unfolded Neutrons to Next Closest Neutron Intensity	76
15.	Ratio between Geant and the experiment.	78
16.	Ratio of peak to base in reference and research spectra.	80

NEUTRON SPECTROSCOPY OPTIMIZATION USING A SOLID STATE THERMAL NEUTRON DETECTOR

1. Introduction

1.1 Overview

The Nuclear Test Ban Treaty signed by President John F. Kennedy in 1963 prohibited the use of nuclear weapons and test detonations in underwater, surface, and space environments. Underground testing was still permitted, however, so long as nuclear fallout did not leave the country. The final pledge was an agreement to migrate towards reduction of all proliferation. Three super powers, the United States, Soviet Union, and United Kingdom, all abided by the treaty. Thirty years later, the United Nations General Assembly produced the Comprehensive Nuclear Test Ban Treaty that 71 nuclear and non-nuclear nations signed. Under this treaty, even underground detonations were banned. President Bill Clinton signed it but the Senate did not endorse it, so the U.S. did not ratify the new treaty [1].

Nuclear weapons are the most fatal weapons on the planet so it was and still is essential to have a stockpile to retain global power. After the Soviet Union collapsed, their nuclear weapon stockpile became insecure with many of its special nuclear material (SNM) left unguarded. Due to the insecurities and despite the reduction of global SNM due to the Nuclear Test Ban Treaty, many people are concerned about the state of the nuclear enterprise and the security of nuclear material in all parts of the world because of the vast variety of terrorist organizations in the world today. The benefit of the treaty is that there are fewer facilities globally producing SNM,

so detector research and technology can be pinpointed to specific research facilities, their designs, and organization. For this reason, the development of new detectors is based on stringent facility specifications, including characteristic signatures from sources and facility infrastructure. Organizations such as the International Atomic Energy Agency (IAEA) have gone to great measures to ensure the security of the world's nuclear stockpile to prevent organizations and countries from obtaining SNM from factories for the proliferation of nuclear weapons.

In a response to the treaties, changing stockpiles, and concerns for proliferation, efforts have been made to replicate SNM spectral signatures at pulsed reactor labs such as the Fast Burst Reactor (FBR) at White Sands Missile Range (WSMR), Sandia Pulsed Reactor (SPR-III), and Aberdeen Proving Ground (APG) in order to study nuclear weapons effects and assess vulnerability. The FBR is the last remaining fast burst reactor in support of the DOE and DoD due to an increase in national security, safety, logistics, and financial concerns involving the manufacturing and support of SNM. Other reactor facilities provide spectral data needed as well to further SNM detection research.

1.2 Motivation

Reactor Facilities and Accelerators

Reactor facilities provide baselines for neutron detector design specifications, and the ones described in this section provide neutron spectral data within 1-10 MeV. This energy group has been particularly difficult to measure because it is often dependent upon low cross section activation foils and energy unfolding but is desired because it includes high energy and above cosmic, terrestrial, and man-made background radiation. Common man-made background sources such as agricultural products, smoke detectors, kitty litter, and road salt are gamma emitters that resemble SNM;

however, they can be differentiated from SNM if high energy neutrons can be detected. High energy neutron sources are also easier to detect because low energy sources are more easily shielded. Signatures produced by SNM are difficult to detect because the gamma and neutron signatures are relatively weak, since the rate of spontaneous neutron decay is low.

Artificial neutron spectra can be produced by reactors and accelerators for detector research. Accelerators require the use of charged particles to accelerate and direct the beam, and nuclear reactors produce neutrons through controlled fission reactions. The FBR is an unmoderated, highly enriched ^{235}U neutron source that replicates fission-type nuclear weapons with neutron energies shown in the Watt spectrum in Figure 1, where the most probable neutron energy from fissioning both ^{235}U and ^{239}Pu is around 1 MeV, the average is around 2 MeV, and the maximum is around 9 MeV. There are a small number of neutrons in the eV range in a Watt spectrum compared to high energy neutrons.

The Annular Core Research Reactor (ACRR) at Sandia National Laboratory (SNL) is a thermal neutron reactor. Like most reactors, the ACRR uses water moderation to produce a neutron beam with very short pulses up to steady-state operation. This qualifies the ACRR for atmospheric neutron tests, whereas the FBR, a metal reactor, simulates the space environment as its neutron energy spectrum provides an unmoderated fission spectrum. Reactors like the ACRR and the Ohio State University Research Reactor (OSURR) demonstrate a lower security threat, as they do not utilize highly enriched uranium (HEU) sources to produce chain reactions. These neutron facilities are considered "thermal reactors" because the moderator is typically light water (^{1}H) which is a strong moderator that quickly reduces the neutron fission energy to thermal. Low atomic number elements like hydrogen are good moderators because of their high scattering cross section.

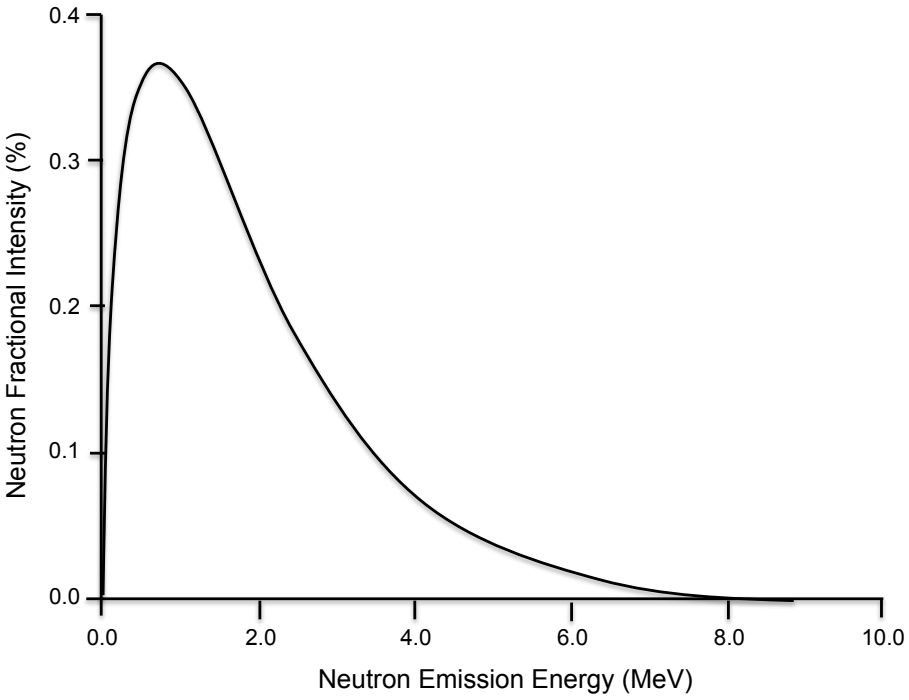

Figure 1. Watt energy spectrum from a fission weapon output.

A large portion of the present research is being placed on the development of high flux and/or high energy accelerators that do not produce SNM like reactors. They are a cleaner, more secure method to produce neutrons for research. Accelerator facilities like the Lawrence Berkeley National Laboratory's (LBNL) Cyclotron and Neutron Radiation Effects Facility (NREF) generate neutrons by the acceleration of charged particles into a conversion material. The LBNL Cyclotron is currently conducting research to configure a customizable energy tuning assembly (ETA) to produce characteristic neutron spectra to a variety of applications instead of relying on moderating materials to less probabilistically produce specific energies after scattering events [2].

At NIF, they are considering pairing spectra from the fusion system with its Godiva bare-sphere uranium reactor to create a superposition of the Watt and fusion spectra thereby more closely replicating the spectrum produced by a thermonu-

clear weapon. The fusion spectrum from common hydrogen isotopes is shown in Figure 2 [3].

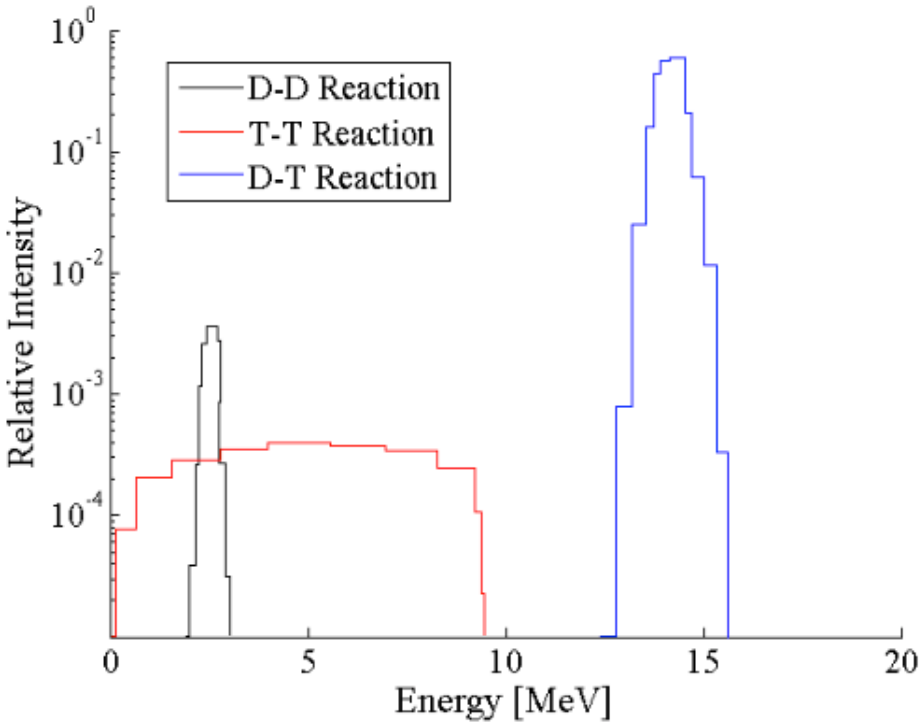

Figure 2. Normalized fusion neutron generator intensities per neutron energy

1.3 Objectives of this Research

A thermal solid state neutron detection experiment was conducted by T. Oakes et al. similar to this research, utilizing high density polyethylene (HDPe) moderating layers to slow the high energy neutrons [4]. The purpose of their research is similar to the project research in regards to developing efficient and portable neutron detectors. Oakes et al. attempted to unfold neutron energies from thermal to 15 MeV; however, they were not able to accurately unfold energies of MeV and above. One limit to their experiment was that their HDPe layers were a single thickness that does not focus on the resolution of neutrons in the MeV range, as opposed to this research. Oakes et al. also used MCNPX 2.6.0 with neutron responses from ^{252}Cf and AmBe

while this research was done using the Geant4.10.1 Monte Carlo particle transport program with a neutron response from a PuBe source.

For the present research, monoenergetic neutrons were moderated in the spectrometer to test the spectrometer response (referring to the layered detector system). This information was later used to unfold the neutron spectra using the Maximum-Likelihood Expectation-Maximization (MLEM) algorithm. Both steps required the use of Geant. The polyengergetic PuBe source was used to demonstrate that the spectrometer could detect and model the PuBe source spectrum. Discrepancies between the Geant and experimental PuBe source spectra were compared and analyzed. The layered spectrometer system with multiple detectors accurately determined which energy neutrons were captured at different layers of the spectrometer. These benchmarks determined the quality and accuracy of the single detector placed at multiple layers.

1.4 Sponsor and Organization of the Thesis

The sponsor for this research is the Domestic Nuclear Detection Office (DNDO). This thesis contains five chapters. Chapter one is the introduction, which provides a background and reasons for pursuing the neutron spectrometer optimization research. Chapter two covers the theory behind neutron moderation and scattering, semiconductor detection, and Monte Carlo particle transport. Chapter three presents the methodology of data collection through the Geant Monte Carlo program and the experimental spectrometer setup with the PuBe source. Chapter four analyzes and compares the data captured in the model and the experiment. Chapter five reviews the research and presents future recommendations for the work.

2. Theory

2.1 Neutron Detection

Neutron detection differs from other detection techniques because neutrons are unaffected by the Coulombic force. These uncharged particles can only be detected by producing charged particles through recoil or absorption interactions that generate a voltage signal proportional to the neutron energy deposited. Recoil detection is primarily done by fast neutrons where neutrons scatter off of atoms in a material, and absorption primarily occurs as the result of slower neutrons following the 1/v principle. Absorption can also produce photons for detection by the photoelectric effect, Compton scattering, or pair production. The following sections address fast and thermal neutron detection with more depth.

Fast Neutron Detection

Fast neutrons are defined as neutrons with an energy above 10 keV [5]. At these energies neutrons primarily interact with media by elastic scattering with target nuclei. Plastic and liquid scintillators are the most common fast neutron detectors that can directly detect fast neutrons by using the result of the elastic collisions in the following way. Because plastic and liquid scintillators are made of low Z materials, fast neutrons can deposit a large amount of energy to the nuclei. This energy results in a highly ionized atom that deposits energy through the Coulombic interactions. The result of these Coulombic collisions is the emission of photons, which are counted using a photomultiplier tube (PMT). The PMT amplifies the signal through a sequence of photocathodes, which provides a signal proportional to the neutron energy deposited.

The advantages of fast neutron detectors is that they are very efficient, approaching 100% efficiency [6], and they are proven to work in the lab setting. The disadvantages, though, are that the cost per detector is high, PMT's are fragile, and the gamma discrimination is fairly low compared to the absorption detectors. The disadvantages limit their use compared to absorption detectors. Recent changes in fast neutron detectors have been achieved, however, by solid state photomultipliers (SSPM's), which are less expensive, have a more compact design, higher resolution, and a higher signal-to-noise ratio [6].

Thermal Neutron Detection

The primary means of neutron detection is absorption, where neutrons interact with a conversion material to convert them to charged particles for detection. Historically, BF_3 and ^{3}He proportional counters, fission chambers, and thin film solid state detectors have been used for absorption detection. Detection is energy dependent and most efficient near thermal neutron energy (0.025 eV) for most elements. Many SNM spectra produce fast neutron spectra and must be slowed down, or moderated, to thermal energies for detection.

After the charged particles are produced by the neutron conversion material, detection occurs in gas filled chambers and semiconductor detectors. In a gas filled chamber, the charged particles deposit their energy by ionization in a gaseous medium. The electrons then produce a charge current from the voltage potential between the anode wire and cathode wall proportional to the deposited energy. Semiconductor detectors operate by energy deposition into a semiconductor material to separate electron-hole pairs in the atomic lattice. The electron current in the conduction band is proportional to the energy deposited by the neutrons. This research utilizes a solid state thermal neutron semiconductor with a ^{10}B conversion material for its high

thermal neutron cross section. The absorption and detection theory are described next.

Conversion Material

Neutrons incident upon a ^{10}B conversion material detector undergo the ^{10}B(n, α)^{7}Li reaction where the resulting Q-value is shown in Equation 1 [7]. Approximately 6% of the reactions lead to the ground state and 94% to the excited state.

$$\text{Q-value of } {}^{10}_{5}B + {}^{1}_{0}n \rightarrow \begin{cases} {}^{7}_{3}Li + {}^{4}_{2}\alpha & 2.792 \text{ MeV (ground state)} \\ {}^{7}_{3}Li* + {}^{4}_{2}\alpha & 2.310 \text{ MeV (excited state)} \end{cases} \tag{1}$$

Abiding by conservation of momentum and solving Equation 2 results in the energies transferred to the lithium-7 and the alpha particles in Equation 3.

$$\begin{aligned} m_{\text{Li}} v_{\text{Li}} &= m_{\alpha} v_{\alpha} \\ \sqrt{2 m_{\text{Li}} E_{\text{Li}}} &= \sqrt{2 m_{\alpha} E_{\alpha}} \end{aligned} \tag{2}$$

$$E_{\text{Li}} = 0.84 \text{ MeV and } E_{\alpha} = 1.47 \text{ MeV} \tag{3}$$

The high Q-value in absorption detectors typically means that the photon discrimination is not a concern since the photons have much lower energy. In addition, electrons can potentially recombine with holes in semiconductor detectors by radiative recombination to produce a photon. Direct bandgap materials may undergo this process via annihiliation, but indirect bandgap materials such as silicon used in this research detector cannot because the conduction and valence bands do not share the same momentum-space. Photons do not carry momentum so conservation of momentum would be violated if radiative recombination occurred in the silicon-based detector.

The neutron detector used in this research is a trench-design solid state thermal neutron detector, shown in Figure 3, that converts neutrons through the ^{10}B(n, α)^{7}Li reaction. The detection efficiency for thermal neutrons in the detector is 22.5% due to the particular structure of the detector and the 99% enriched ^{10}B, whose thermal neutron cross section is very high, approximately 3866 barns [8]. The trench design provides a higher intrinsic detection efficiency of the converted charged particles because the pn junction is on three of four sides of the conversion reaction unlike standard planar semiconductor detectors [6]. The electric field created by the pn junction produces an electron current proportional to the deposited neutron energy. Semiconductor physics is discussed in the following section.

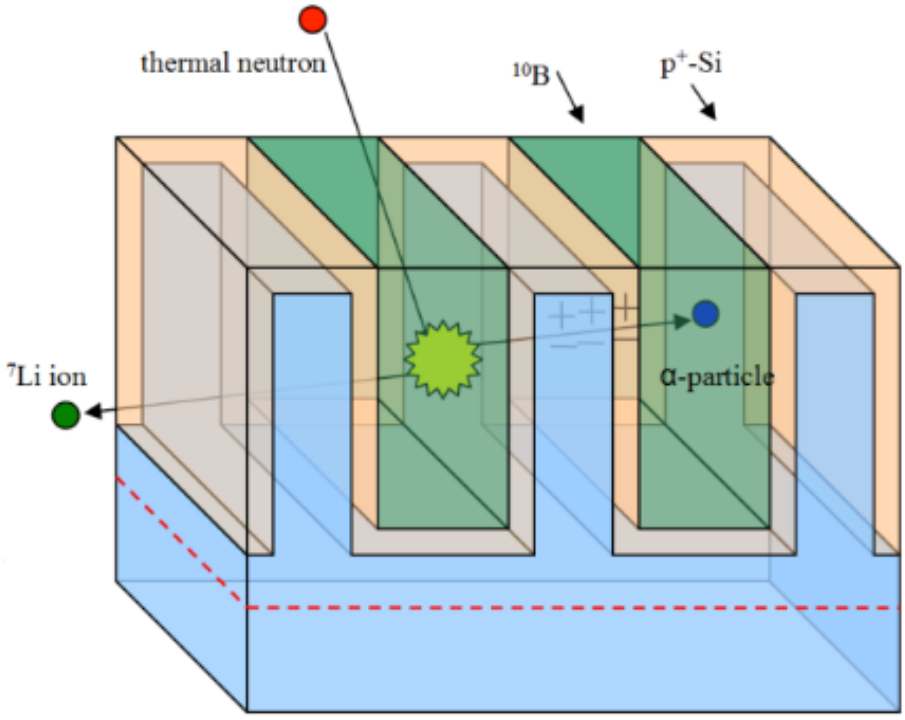

Figure 3. The trench design neutron semiconductor detector is an efficient conversion particle detector due to the semiconductor material placed on three of the four sides. The width of the trench depends on the range of the charged particles' range.

Semiconductor Physics

Electron-hole Pair Representation in Semiconductors

Silicon is the most common semiconductor material. It contains four electrons providing a very efficient way to covalently bond with itself. The electrons remain in their covalent bonds at low temperatures, but as the temperature rises the electrons gain enough thermal energy to escape into the conduction band. This leaves a gap in the silicon bonds known as a hole. The electrons still bonded in the lattice are able to move to the holes where the conduction band electron once was.

Drift Current

Carrier drift is the motion of a charged particle as a result of an electric field. By convention, positively charged particles move in the direction of the electric field and vice versa for negatively charged particles. Holes and conduction electrons are the relevant charge carriers for semiconductors. Carrier motion on a microscopic scale is extremely complex due to the high number of scatters in the carriers' paths; however, the drift current on a macroscopic scale is interpreted linearly. The drift current and current density for a hole are shown by Equations 4 and 5.

$$I_{P|drift} = qpv_dA \tag{4}$$

$$J_{P|drift} = qpv_d \tag{5}$$

I is the drift current, J is the current density where $J = I/A$, q is the charge, p is the hole concentration, v_d is the drift velocity, and A is the cross sectional area where the charge is travelling. The current density can also be written by Equation 6, addressing the more intrinsic properties of the charge carriers in the semiconductor.

$$J_{P|drift} = q\mu_p\xi \tag{6}$$

μ is the carrier mobility, or freedom of carrier movement, and ξ is the electric field.

Diffusion Current

Particles of high concentration diffuse to lower concentrations and continue to do so until equilibrium is reached. For diffusion to occur, there must be a spacial particle gradient. A larger gradient means that the flux of particles entering a region is larger and represented by Fick's law in Equation 7, and the diffusion current density is achieved by multiplying the flux by the carrier charge in Equation 8.

$$\phi = -D\nabla p \tag{7}$$

$$J_{P|diff} = -qD_p\nabla p \tag{8}$$

ϕ is the flux and D is the diffusion coefficient. Holes are used as opposed to the interchangeable electrons. Total current densities in a semiconductor are obtained by adding the drift and diffusion current densities in each of the p- or n-type regions represented by Equation 9.

$$J_P = J_{P|drift} + J_{P|diff} = q\mu_p\xi - qD_p\nabla p \tag{9}$$

Recombination-Generation

Recombination refers to the action of the electrons filling the place of a hole, or elimination of the electron-hole pair. Generation refers to the creation of electron-hole pairs. Recombination and generation (R-G) play a significant role in semiconductor technology since devices are rarely in equilibrium due to the constant R-G of electron-

hole pairs. While there are multiple processes for both recombination and generation, only the most common processes are described in this document.

Band-to-band recombination refers to the process by which an electron in the conduction band travels by a hole in the valence band. A photon is typically a result as shown in Figure 4-a. R-G center recombination occurs when impurities are located in the semiconductor material so that lattice defects are present. This introduces electronic levels within the forbidden region near midgap between the valence and conduction regions shown in Figure 4-b.

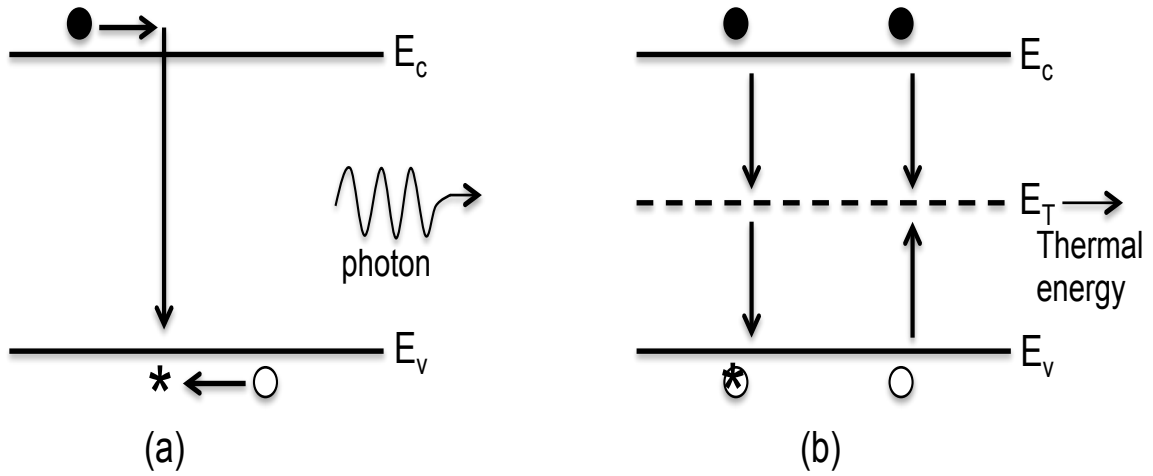

Figure 4. (a) Band-to-band recombination; (b) R-G center recombination

Generation is fundamentally the reverse action of recombination. For every recombination process there can also be generation. Band-to-band generation can be induced by light, called photogeneration, or thermal energy, called direct thermal generation. R-G centers can act as thermally activated spaces for electrons to jump to the intermediate space and then to the conduction band, which is called R-G center generation. Generation methods are shown in Figure 5.

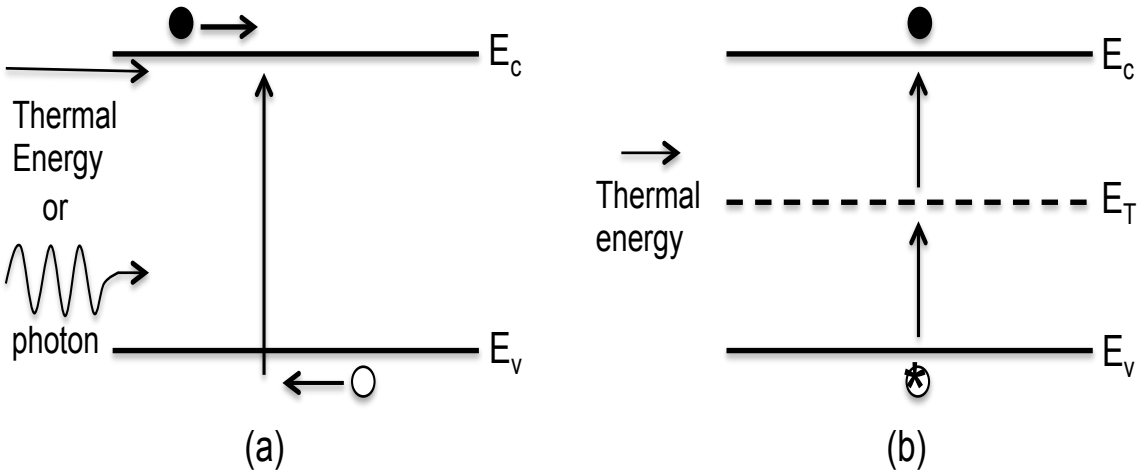

Figure 5. (a) Band-to-band generation; (b) R-G center generation.

PN Junctions

A pn junction is formed when an n-type and p-type semiconductor are in contact. When these materials are joined, the electrons diffuse to the p-type side and the holes diffuse to n-type side. Due to the diffusion and recombination process, the electrons and holes leave behind negative acceptor and positive donor ions that create an electric field. This is called space charge. Equilibrium is reached when the electric field is strong enough and the electron or hole currents are equal. The depletion region width is given by Equation 10 [9]. The exchange of charge in a semiconductor is thus denoted by the drift and diffusion of the charge carriers. The potential over the depletion region, or the built-in potential, is given by integrating the electric field over the depletion region. The net current density in a p-type material, where p- and n-type can be interchanged, of a pn junction is given by Equation 11.

$$W = x_p + x_n = \sqrt{\frac{2\varepsilon}{q} V_0 \left(\frac{1}{N_A} + \frac{1}{N_D} \right)} \tag{10}$$

$$J = \sigma \xi - D \nabla qp \tag{11}$$

W is the depletion width, x_p and x_n are the distances into each bulk material the depletion region extends, ε is the permittivity of free space, V_0 is the built-in potential, N_A and N_D are the acceptor and donor atom concentrations, σ is the conductivity, D is the diffusion coefficient, q is the charge by an electron or hole, and p is the concentration of holes in the p-type material. The hole concentration can be substituted for electron concentration in the n-type material.

Poisson's equation is the base to solving the electrostatic variables of the pn junction. The junction is a 1-dimensional problem so Poisson's Equation is taken from the 3D Equation 12 to the 1D Equation 13, and the charge density is presented in Equation 14.

$$\nabla \cdot \xi = \frac{\rho}{K_s \varepsilon_0} \tag{12}$$

$$\frac{d\xi}{dx} = \frac{\rho}{K_s \varepsilon_0} \tag{13}$$

$$\rho = q(p - n + N_D - N_A) \tag{14}$$

ρ is the charge density and K_S is the dielectric constant in the semiconductor. An electric field exists in the depletion region due to the imbalance of positive and negative ions and the lack of an electric field in the bulk regions due to the consistency of a high concentration of electrons in the n-region and a high concentration of holes in the p-region.

The depletion region is drawn in greater detail in Figure 6 to provide an idea of how the variables change in space. The solid lines represent the depletion width under equilibrium conditions with no bias voltage. The dotted lines represent the depletion width under positive and negative voltages, or forward and reverse bias, respectively.

The forward and reverse biases decrease or increase the electric field within the junction, respectively. A forward bias is applied by connecting a positive voltage

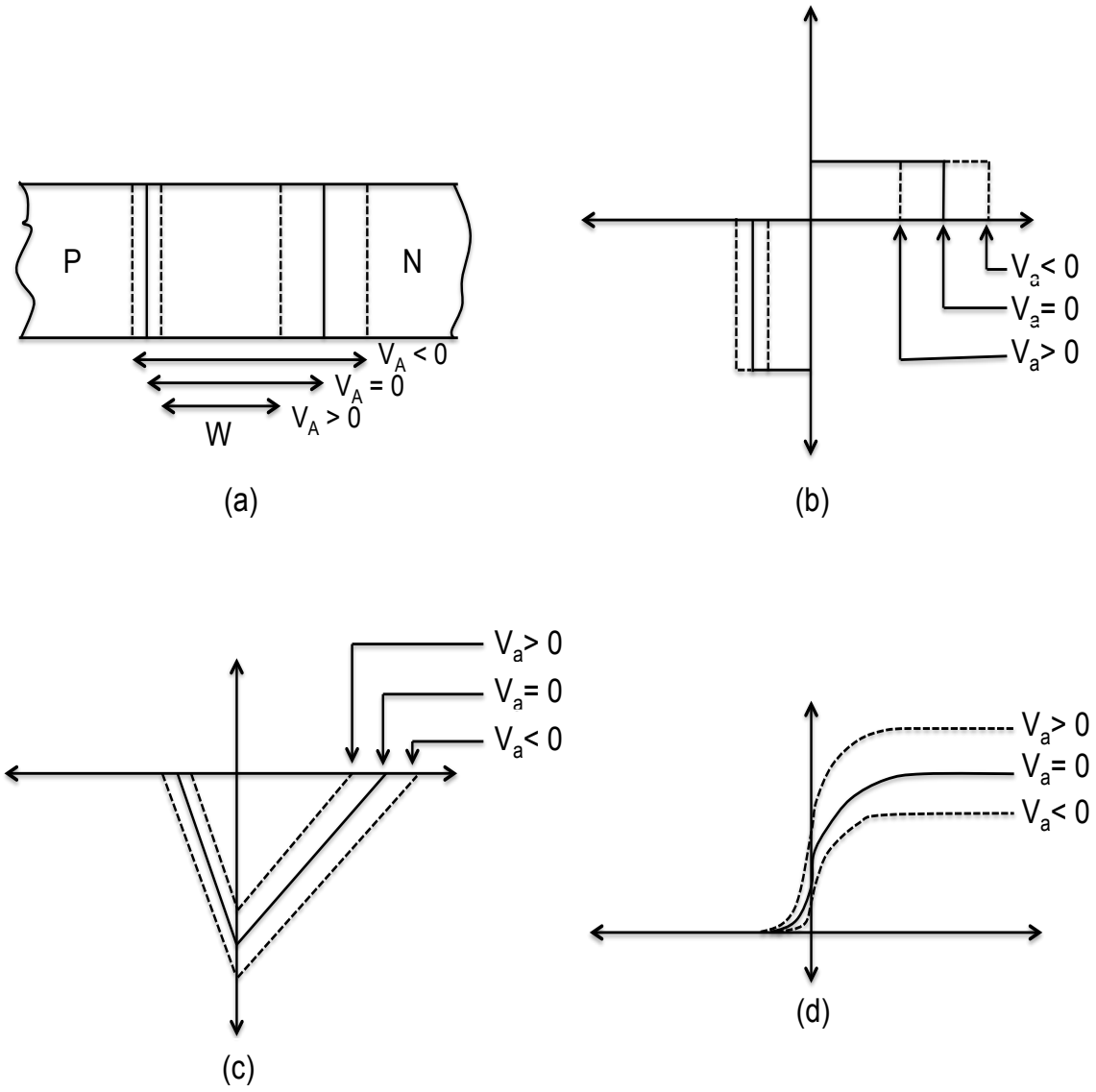

Figure 6. The impact of forward and reverse biases in comparison with a zero bias system at equilibrium in a pn junction.

to the p-type region and a negative voltage to the n-type region, so the holes and electrons move away from the bulk regions toward the junction. This decreases the depletion width so less space charge is created , which decreases the electric field and potential. A higher diffusion current arises from the decreased depletion width, while the drift current remains relatively unchanged because it depends on the number of charge carriers produced within a diffusion length inside and close to the depletion region, and the depletion region is only reduced a minute distance.

The opposite actions take place in the reverse biased junction because a negative voltage is applied to the p-type region and a positive voltage to the n-type region. Now, the charge carriers flow in the opposite direction as they did in forward bias, so the depletion region increases and thus the electric field and potential increase. Consequentially, the diffusion current decreases and the drift current remains relatively unchanged again but increases due to the small increase in the depletion region. It is important to recognize the diode equation in Equation 15.

$$I = I_0 \left(\exp\left(\frac{eV}{k_B T} \right) - 1 \right) \tag{15}$$

While in forward bias ($V_A > 0$), there is an exponential increase in current; while in reverse bias ($V_A < 0$), the current remains neutral until a drop-off occurs. This drop-off is called breakdown and is caused by either avalanching or quantum tunneling through the bandgap. Heating by the overloading current and voltage are sufficient to damage the device so that a heat sink is needed [10].

2.2 Neutron Moderation

In this research, a solid state thermal neutron detector was used to detect fast neutron sources, so moderation was required. Neutron moderation is the foundation of this research. The objective is not only to moderate neutrons but to do so while

minimizing losses in order to be able to unfold the spectrum to identify a known or unknown source.

A solid state spectrometer was optimized with high density polyethylene (HDPe) moderator layers. The HDPe has a high moderating ratio, the ratio of neutron scattering to absorption, due to the high scattering cross section of hydrogen. Neutrons are absorbed within HDPe which decreases the number of detected neutrons, which also decreases efficiency because neutrons cannot be detected. Elastic scattering in the HDPe is the primary neutron interaction, however. If there is too much moderating material, neutrons will be lost by absorption within the moderator. Increasing the thickness of the moderators increases the number of neutron collisions, so higher energy neutrons can slow to thermal energies before they reach a detector.

Scattering and Moderation

Average Logarithmic Energy Decrement

The average logarithmic energy decrement per neutron collision on a target is energy independent and defined by Equations 16 to 18. The commonly used approximation is Equation 18 [11].

$$\xi = 1 + \frac{\alpha}{1-\alpha} \ln \alpha \tag{16}$$

$$\alpha = \left(\frac{A-1}{A+1} \right)^2 \tag{17}$$

$$\xi = \frac{2}{A + 2/3} \tag{18}$$

Equations 16 to 18 are valid for element moderation, but when compounds are moderated, scattering microscopic cross sections are needed for individual elements

in the compound. This makes ξ energy-dependent because the element ξ is calculated by integrating over energy. When compounds are present, ξ is weighted by its cross sections, making x_i energy dependent. The formula used for compounds is shown in Equation 19.

$$\xi_{compound} = \sum_{i=1}^{N} \frac{\xi_i \sigma_i}{\sigma_i} \tag{19}$$

N is the total number of elements in the compound and i is the specific elements in the compound [12]. There are two elements in the CH_2 HDPe, hydrogen and carbon.

Source Energy

The neutron spectrum aids in understanding approximately how many collisions is required to slow down the neutrons in the spectrum to approximate the ideal thickness of the moderator material that allows for the detection of the most neutrons from the source. Monoenergetic neutrons follow this analytical method. Otherwise computational methods are needed. An example, relevant to this work, is the deuterium-deuterium (D-D) reaction with 2.45 MeV neutrons emitted. The microscopic cross sections at this energy were collected using the Evaluated Nuclear Data File (ENDF) through the National Nuclear Data Center (NNDC) archive source [8]. Table 1 lists scattering microscopic cross sections for hydrogen and carbon at 0.025 eV and 2.45 MeV. The average logarithmic energy decrement for HDPe is shown in Equation 20.

Table 1. Scattering microscropic cross sections at thermal and D-D reaction neutron energies.

Energy	0.025 eV	2.45 MeV
$\sigma_{s,hydrogen}$ (barns)	30.508	2.582
$\sigma_{s,carbon}$ (barns)	4.945	1.586

$$\xi_{HDPe} = \frac{(0.158)(1.586) + 2(1)(2.582)}{1.586 + 2(2.582)} = 0.802 \tag{20}$$

$i = 1$ in Equation 20 is carbon and $i = 2$ is hydrogen.

Mean Free Path

The mean free path λ of a particle is the distance it travels in a material medium before it interacts with the material lattice. For instance, the mean free path of a neutron is the path the neutron travels before it undergoes elastic scattering, inelastic scattering, or absorption. The mean free path is defined by Equation 21.

$$\lambda = 1/\Sigma_t \tag{21}$$

Σ_t is the total macroscopic cross section, the sum of the scattering and absorption macroscopic cross sections. Low Z elements generally have low absorption cross sections and high scattering cross sections, so the total is usually closely equivalent to the scattering cross section. The macroscopic cross section is expressed by Equation 22.

$$\Sigma = N\sigma = \frac{\rho N_A}{M}\sigma \tag{22}$$

N is the number density, ρ is density, N_A is Avogadro's number, and M is the atomic mass. $\Sigma_t = 0.273$ cm^{-1} for a 2.45 MeV, which translates to $\lambda = 3.663$ cm. On the other hand, a thermal neutron has $\Sigma_t = 2.667$ cm^{-1} and $\lambda = 0.375$ cm. Selecting another arbitrary energy of 1 MeV with $\Sigma_t = 0.448$ cm^{-1} and $\lambda = 2.23$ cm, a fitted plot of mean free path versus energy was made in MATLAB shown in Figure 7 to visualize how energy affects the neutron path; the trend line is lightly quadratic with a downward concavity. The interpolated fit values closely resemble the actual

data from ENDF. Table 2 shows the mean free path for several energies of interest. Figure 8 is the microscopic cross sections for hydrogen and carbon, where carbon has more resonance peaks and hydrogen has a general trend that is easily observed per energy [13].

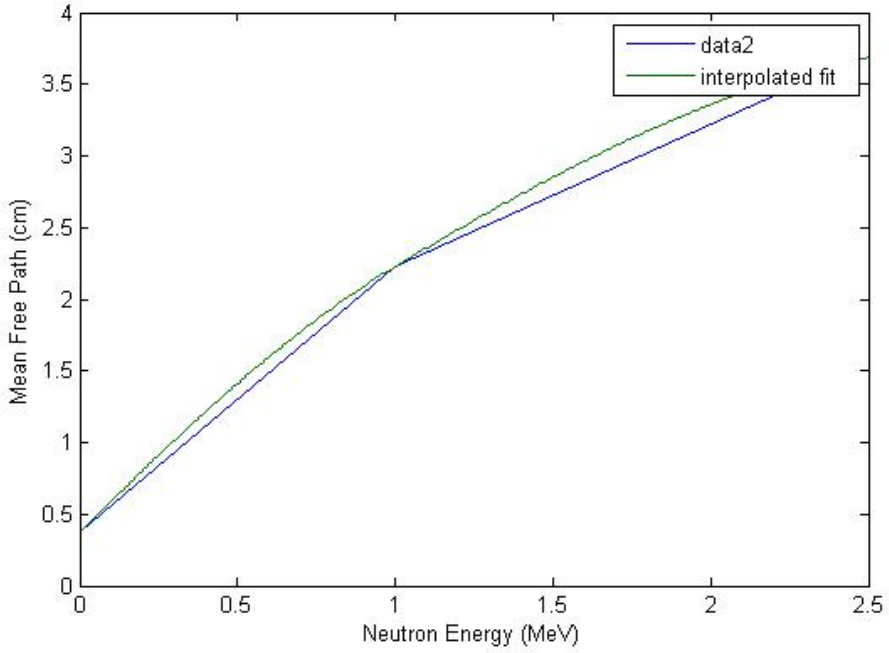

Figure 7. Mean Free Path vs Neutron Energy. The trend is decreasing quadratically.

Table 2. Several values for neutron energies and their mean free paths.

Energy (MeV)	1.0×10^{-7}	0.25	0.5	1	1.5	2
Mean Free Path (cm)	0.3731	0.9115	1.4116	2.2272	2.8498	3.3581

Number of Collisions

A neutron's lethargy, μ, is logarithmic energy decrement, or "laziness," of a neutron as it travels through any medium while losing energy through scattering and is shown in Equations 23 and 24 [11].

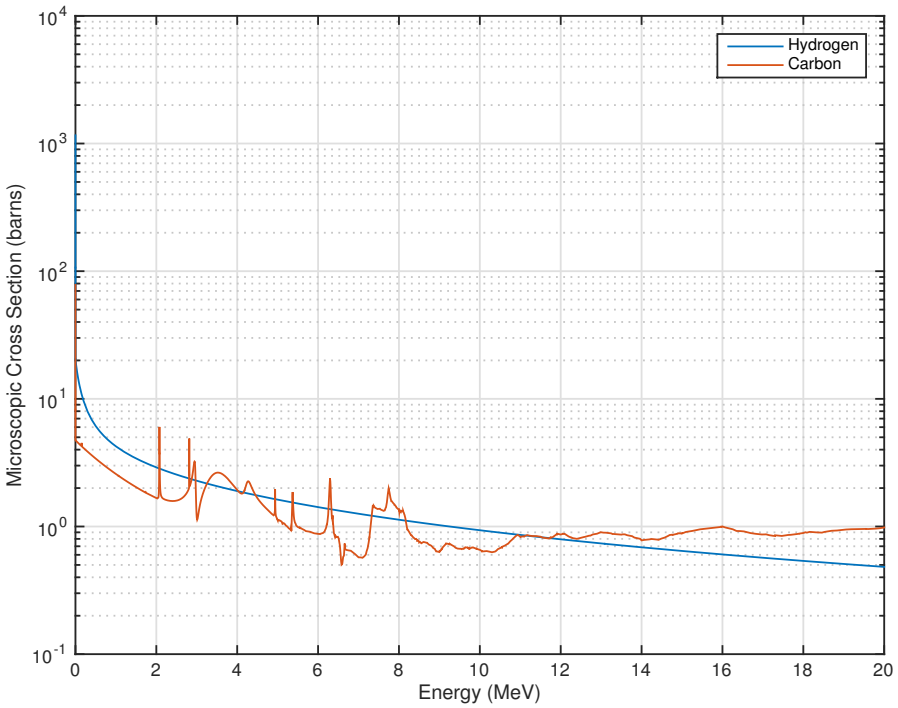

Figure 8. Carbon microscopic cross section versus energy. The x-axis is on a linear scale [ENDF].

$$E = E_0 e^{-\mu} \tag{23}$$

$$\mu = \ln\left(\frac{E_0}{E}\right) \tag{24}$$

E_0 is the initial energy, and E is the final energy after scattering but is thermal for this experiment due to the efficiency of thermal neutrons for the detector. The average number of collisions, n, to reach energy E utilizes the average logarithmic energy loss and the neutron lethargy terms in Equation 25.

$$n = \frac{\mu}{\xi} \tag{25}$$

Moderation in a Material Medium

Applying the 2.45 MeV D-D fusion neutron to an HDPe target, $n \simeq 23$ collisions. Just as lower Z elements scatter neutrons as opposed to absorbing them, they also require fewer collisions to thermalize a neutron. This is because more energy can be transferred to a smaller nuclear mass than a larger one. Figure 9 references polyethylene moderation compared to heavier elements. Because its chemical makeup is carbon and hydrogen and thus contains only low-Z elements, neutrons do not travel very far before being heavily moderated. The number of collisions is highly probabilistic, so this is a rough estimate of what actually occurs.

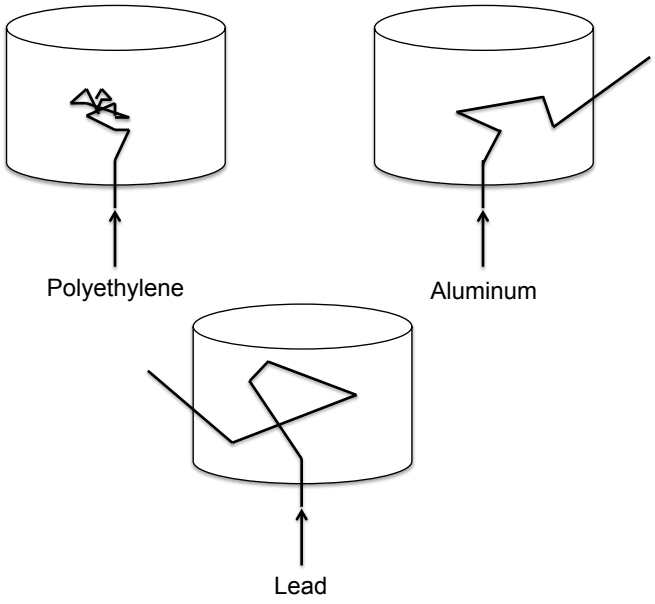

Figure 9. Light elements moderate neutrons in shorter distances. A greater amount of energy can be transferred to polyethylene atoms. Neutrons will travel further in aluminum and lead because of the higher atomic mass [13].

Due to the highly probabilistic neutron path within a medium, it is impossible to analytically solve exactly how much moderating material is needed to thermalize a neutron. If the scattering angles were all minimized (close to zero degrees) so the energy transfer was near linear in space, the thickness of HDPe needed to thermalize

a neutron for thermal neutron detection would be defined by multiplying the number of collisions by the mean free. For a 2.45 MeV neutron, the fraction of energy lost per collision is 0.448 as shown in Equation 26.

$$x = f \sum_{i=1}^{N} \lambda_i = 19.67 \text{ cm}, \quad f = 0.448 \tag{26}$$

Here, x is the distance a neutron must travel to thermalize and f is found by solving for thermal E in Equations 23 - 25 from a single collision. The result from Equation 26 is unrealistic because neutron paths are nonlinear and scattering angles are inversely proportional to energy. If scattering angles remained near zero, like those angles from high energy neutrons, then the distance would be closer to 19.67 cm. As the neutrons slow to thermal energies, the distance they travel through a good moderator becomes small; therefore, when modeling neutron moderation, faster neutrons travel much further into the moderator.

It does not take many collisions to reach energies that will cause larger neutron scattering angles. Table 3 lists the number of collisions from 2.45 MeV to reach certain neutron energies. This data suggests that few collisions are required to slow neutrons to speeds that induce large scattering angles, according to the differential cross section data in the ENDF [8]. This theory is supported by the Geant particle transport simulations, referenced in the Chapter 3, by modeling the appropriate thicknesses to moderate and later unfold the neutrons from fast neutron sources.

Table 3. Number of collisions to reach a specific energy from 2.45 MeV.

E_n	1 MeV	100 keV	1 keV	100 eV	1 eV
$\sim$ n	1	4	10	12.5	18

3. Methodology

The root of this research is to unfold a response function from an unknown source, and it can also be used to unfold a known source depending on research goals. The unfolding routine used is the MLEM method requires three parameters to appropriately unfold a spectrum: 1) a response function, 2) source data, and 3) and an initial guess which will produce a solution spectrum. The first and second parameters required the use of the Monte Carlo method applied to particle transport. The optimized response function was developed by irradiating monoenergetic neutrons at the spectrometer and the response by a polyenergetic source, which is referred to as 'source data' in this paper. It was developed by irradiating polyenergetic neutrons at the spectrometer with the optimized response function data. The final parameter does not require extensive research on prior spectra data for an initial guess and can be any value above zero. The response function was employed in an experiment that collected neutron counts from the source with the response function data. This data was used to compare the MLEM unfolded model and experiment spectra.

This chapter explains the development of the MLEM method by first discussing the general reconstructive iterative process and then MLEM, including the three key parameters to solve it. The Monte Carlo method follows, which was used to develop the first two of the three parameters. Specifically, the Geant particle transport program was used to created neutron response functions by optimizing layered HDPe thicknesses. The optimization approach is discussed to explain the steps to optimize HDPe thickness. A PuBe source was used for the polyenergetic source data to unfold the solution spectra using the previously solved optimal thickness combination. The unfolding algorithm is examined along with a simple example that shows several iterations and a solution. The equipment and experimental methods are discussed after the modeling procedure is described. It addresses signal amplification, counting

mechanisms, and semiconductor detector principles. Lastly, safety is an issue when handling neutron radiation and is applied by concrete to scatter and absorb the neutrons.

3.1 Maximum-Likelihood Expectation-Maximization Unfolding

The goal of the research is to produce a neutron spectrometer that will be able to capture neutrons from a polyenergetic source and consequently be able to unfold the spectrum, or identify the neutron source energy intensities. The MLEM method is an iterative method that is able to take a set of data with observed and unobserved, variables to produce a maximum likelihood function. It is important to optimize data to maximize the likelihood of the matrix solution.

General Reconstructive Iterative Methods

The MLEM and other reconstructive iterative methods have been seen in medical physics in positron emission tomography (PET) and single photon emission computed tomography (SPECT) for examples. There are several iterative methods for selecting the best solutions but they all have common similarities. Figure 10 shows the general iterative approach to find the solution. Generally, an initial guess to the solution matrix is implanted into the system. The projection step is applied to the current estimate to calculate a new estimate, which will be used as the current estimate in the next iteration until optimal. The projection is modified after comparison with the experimental or source values. The difference between the previous and current guess values are called residuals, or projection-space error values, which are then 'back-mapped' and the system updated and a new matrix estimate produced. The process continues until the difference between error values is minimal so the best matrix solution is produced. A variety of reconstructive iterative methods are drawn

from the differences between the projection, comparison, backprojection, and updates in the cycle [14].

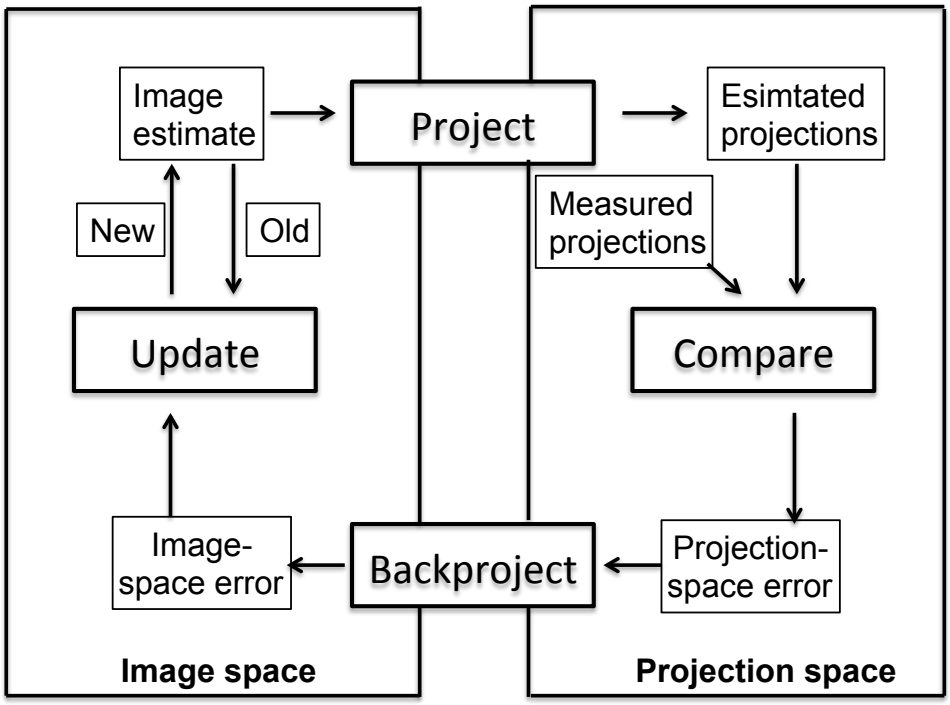

Figure 10. Reconstruction process for the general iterative reconstruction [14].

MLEM Reconstruction

The reconstructive iterative method selected for this research is the MLEM method and is presented as problem solving to an incomplete dataset. MLEM was developed in 1977 [15] and is a statistical analysis tool meant to create other algorithmic tools rather than act as a tool in itself. PET and SPECT and astronomical imaging are popular imaging methods where MLEM is used, and it has been recently applied to spectrum unfolding. The MLEM formula is specified in Equation 27.

$$\lambda_j^{n+1} = \frac{\lambda_j^n}{\sum_{i'}^{N} A_{i'j}} \sum_{i}^{N} A_{ij} \frac{Y}{\sum_{k}^{L} A_{ik} \lambda_k^n} \tag{27}$$

In Equation 27, λ is the initial guess and matrix solution, A is the response function, and Y is the source data which will all be discussed below.

MLEM is comparable to the general iterative process described in the general reconstruction above; the comparison is shown analytically in Figure 11. It is differ-

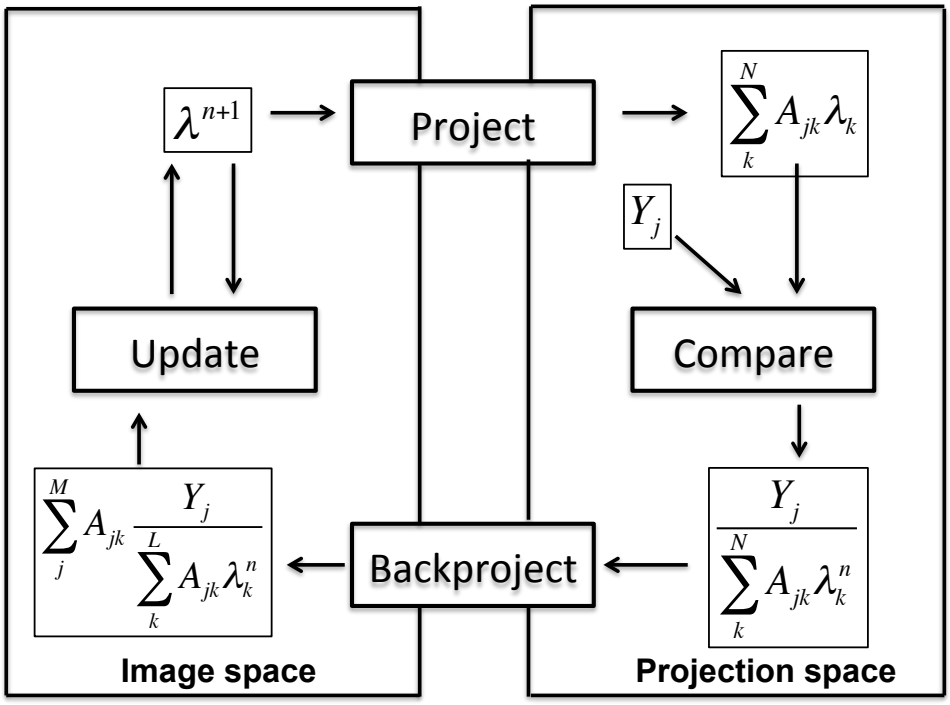

Figure 11. Reconstruction process for the MLEM iterative reconstruction [14].

ent than most other methods because the solution matrix is updated simultaneously and the convergence of the solution is expected. Two negatives with MLEM are the computation time and the noise associated with convergence [14], especially visible in imaging techniques where the variance of process increases with the convergence. Determining the point of termination of the MLEM process may require some skill but it provides good results even if the reconstruction is discontinued early. This may exclude unnecessary variance in the process, which may ultimately provide better results unless a specific termination point works; specific termination points are usu-

ally assessed based on the research and experiment being conducted. The parameters needed to solve the MLEM method are as follows:

1. Response function A (matrix: detector number by energy bin)
    - This research: response of counts per neutron energy group per detector
2. Source data Y (matrix: detector number by one)
    - This research: response of all source energy intensities of a polyenergetic source 'smeared' over all detectors
3. Initial neutron spectrum guess λ (matrix: energy bin by one)
    - This research: any positive values

The benefit of MLEM is that the initial guess does not need to be accurate or from any database so long as it is positive. Whereas, other unfolding methods need an estimated initial neutron spectrum guess. The development of the neutron responses was done by the Monte Carlo method.

3.2 Monte Carlo Method

Monte Carlo simulations utilize random numbers to produce probability distributions to model highly probabilistic natural events. It is a very useful tool in many fields including medical physics, finance, economics, nuclear engineering, and others. It provides modeling confirmation to experimental and natural phenomena through statistical analysis.

The Monte Carlo system operates through the use of probability density functions (PDF's); a random number generator that distributes these values by their PDF; sampling populations from PDF's; scoring to tally important quantities; error estimation

to decipher the statistical variance of a distribution function; and variance reduction to reduce computational time and effort by reducing variance in the simulated output solution. It takes uncertainties within an input and calculates expected outputs through models. It is a method of calculating uncertainties through probability distributions. Since it is a system of probabilistic inputs, the outputs are averages of the likelihood of events occurring.

Monte Carlo quantifies event occurrence by saying, for example, that if someone opened a textbook, there will be a 30% chance that person flips to a page between 300 and 400. There are other methods to propagate statistical uncertainties but Monte Carlo is a powerful method for quantifying large histories of events. Simulations are modeled many times all with an equally random probability. This improves the statistical accuracy and precision of the desired or expected outcome. All parameters of the test simulation are sampled from specific distributions according to their own parameter subsets and over time. The results of the parameters are independent of each other and classified as probability distributions. This research is based particularly on Monte Carlo particle transport methods [16].

Random Variables

There are two types of random variables used in statistical analysis, single continuous random variables and discrete random variables. The statistics in this document refer to single continuous due to the nature of the research. Discrete random variables will be discussed briefly and only where specifically mentioned. In this discussion, x is a single continuous random variable on some interval. Because x is random, mathematically it will be treated in terms of probability by Equation 28.

$$P\{x_i \leq X\} \text{ or } P\{E\} \tag{28}$$

In Equation 28, x_i is the observed value on an X specified value and E is an event which also takes on a probability, which can be represented by the example above of opening to a page in a textbook. A probability density function (PDF) of a random variable takes on three characteristics as follows.

1. Defined on interval $[a, b]$, where $b > a$.

2. Non-negative or zero on the interval [a, b].

3. Normalized by Equation 29.

$$\int_a^b f(x)dx = 1 \tag{29}$$

In Equation 29, a and b are real numbers from $a \to -\infty$ to $b \to \infty$ and the intervals are open or closed.

Probability Density Function

PDF's associate a probability given a unit of x where the PDF $f(x)$ is in inverse units of x. Continuous random variables are classified as such because they can take on an infinite number of solutions. Consider that there is a probability that a soccer player kicks a soccer ball at a goal post and the ball deflects from the post at an angle. The question asks for the probability that the soccer ball will deflect at an angle between 80 and 85 degrees. There is an infinite number of angles that the ball can scatter, for instance 82.385273 degrees; thus, the problem becomes a continuous random variable. In other words, $f(x)dx$ defines the probability that a random sample x_i will fall within dx on x, where x is the infinite range of values the problem may accept. In the last example, the range of values the soccer ball can scatter is from 0

to 360 degrees. The probability is described by Equation 30.

$$f(x)dx = P\{x \leq x_i \leq x + dx\} \tag{30}$$

Discrete random variables on the other hand are used when there are not an infinite number of solutions available. For example, a stack of 52 cards is stacked to build a card house. What is the probability if someone blew on the card house, that a certain number of cards would fall and the rest continue to stand. Only a specific number of cards can fall in this scenario. The PDF $f(x_i)$ of discrete random variables is a probability that an event i will occur, where i takes on integer values 1, 2, 3,...,I. The PDF and CDF is given by Equations 31.

$$f(x) = P(x = x_i) \tag{31}$$

Cumulative Density Function

The cumulative distribution function (CDF), or $F(x)$, is a measure of the accumulating probability from a lower limit a to the random sample variable x_i, so the distribution of the function is always increasing until the function reaches a selected x along the function from a to x_i. A CDF takes the form of Equation 32.

$$F(x_i) = P\{a \leq x \leq x_i\} \tag{32}$$

It can be expressed by the integral in Equation 33.

$$F(x) = \int_a^x f(x')dx' \tag{33}$$

Here, $f(x)$ is again the PDF over the interval $[a, b]$. The discrete function is expressed by Equation 34.

$$F_i \equiv \sum_{j=1}^{i} f_j \tag{34}$$

A common example is the radioactive decay of the number of isotopes remaining from decay after a certain period of time has elapsed. Nuclear physics takes the familiar form of Equation 35.

$$\frac{dN}{dt} = -\mu N \tag{35}$$

The solution to this first order, linear differential equation is in Equation 36.

$$N(t) = N_0 e^{-\mu t} \tag{36}$$

Here, N_0 is the initial amount of a particular isotope, λ is the decay constant, and t is the elapsed time. The PDF is expressed as a general form of exponential decay pertinent to more mathematical and scientific applications and takes the form of Equation 37.

$$f(x) = \mu e^{-\mu x} \tag{37}$$

Here, μ is a general decay factor known as the rate parameter. In the following example, the rate $\mu = 0.25$. The CDF of the function is shown in Equation 38.

$$F(x) = 1 - e^{-\mu x} \tag{38}$$

Figures 12 and 13 show the PDF and CDF for the general exponential attenuation problem in Equation 35.

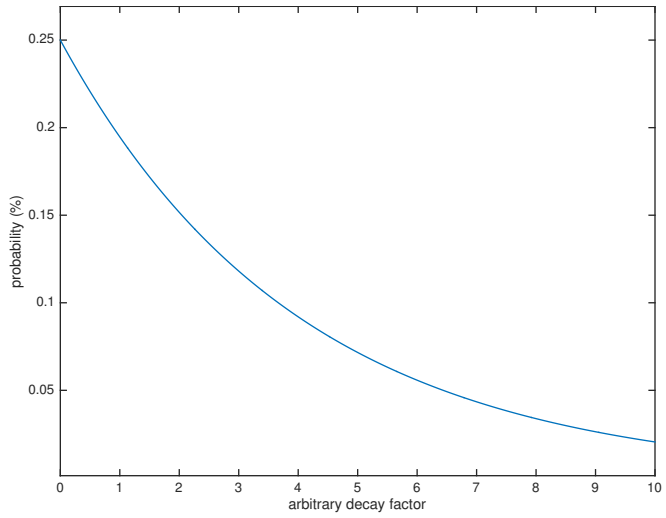

Figure 12. PDF for a general exponential decay problem

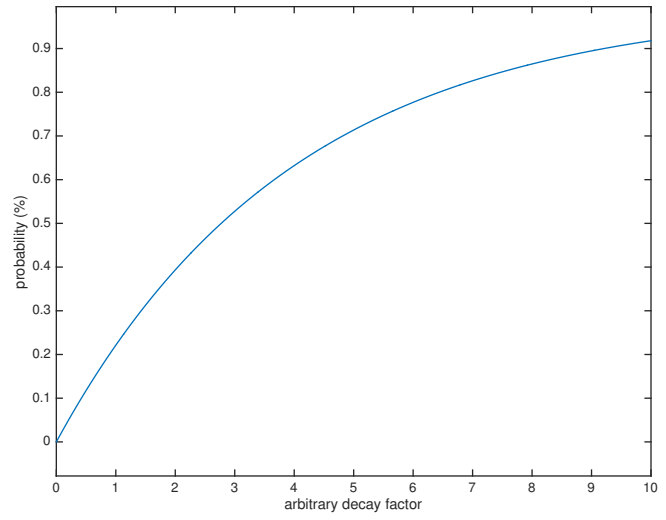

Figure 13. CDF for a general exponential decay problem

To determine the sample variable x of the non-normalized function from the random variable r on the normalized plot where $0 \leq r \leq 1$, the CDF $F(x)$ is set equal to r and solved for x demonstrated by the use of Equations 39.

$$\begin{aligned} F(x) \equiv r &= 1 - e^{-\mu x} \\ x &= -\frac{\ln(r)}{\lambda} \end{aligned} \tag{39}$$

Mean, Variance, and Standard Deviation

Mean μ, variance σ^2, and standard deviation σ are a statistician's most basic tools. They will be discussed briefly but they play an invaluable role in the context of Monte Carlo. Essentially, they are a measure of the statistical reliance of a PDF. The mean solves the average value, or expected value, of a probability distribution or random variable x and defined by 40.

$$\langle x \rangle \equiv E(x) \equiv \mu(x) \equiv \int_a^b x f(x) dx \tag{40}$$

The mean when described later in the scoring section will be labeled with a z instead of an x to imply the difference between the random variable and it's sample mean. The variance measures the variation in the distribution of random variable x and is defined by Equation 41, simplified by 42.

$$\sigma^2(x) \equiv \left\langle [x - \langle x \rangle]^2 \right\rangle = \int_a^b [x - \langle x \rangle]^2 f(x) dx \tag{41}$$

$$\sigma^2(x) = \left\langle x^2 \right\rangle - \langle x \rangle^2 \tag{42}$$

The variance is the square of the standard deviation and only takes the magnitude into consideration, whereas the standard deviation, σ, considers the direction and magnitude.

The general attenuation formula shown in Equation 37 is used in following example. The mean lifetime is shown by Equation 43.

$$\langle t \rangle = \mu \int_0^\infty t e^{-\mu t} dt = \frac{1}{\mu} \tag{43}$$

The population variance is associated by Equation 44.

$$\sigma^2(t) = \int_0^\infty (t - \langle t \rangle)^2 \, p(t) dt = \left\langle t^2 \right\rangle - \langle t \rangle^2 \tag{44}$$

$$\left\langle t^2 \right\rangle = \int_0^\infty t^2 \, p(t) dt = \frac{2}{\mu^2} \tag{45}$$

Sampling and Scoring

Sampling is the process by which random numbers are collected and are governed by a given function. In theory, the random samples should collectively reproduce the function by which they are governed. Because Monte Carlo is governed by statistics, a larger number of collected samples will recreate the function with higher precision and accuracy. Scoring is an estimation process to solve for the expected value of a random variable. The score represents the average $z(x_i)$ from the number of samples i.

Sampling

Monte Carlo simulations make use of random number generators in computer programs; however, these numbers are not precisely random. Generators use algorithms to produce their own specific long, complicated arrays of numbers that undergo a

variety of statistical tests. These are used to produce pseudorandom numbers ρ_i, which is integral to the process of sampling. This document will use r_i as the random number so as to avoid confusion. There are a variety of sampling methods that can be used. The common rejection method defines the region under a closed $f(x)$ within x-axis limits $[a, b]$ and y-axis limits $[0, M]$ as acceptable x_i values, whereas the values above it are not accepted and thus rejected. The two basic steps to recover a x_i from $f(x)$ are as follows:

1. Select random x_i where $x \epsilon [a, b]$ and $x_i = r_i(b - a) + a$. If this falls within the defined limits, except the selected random x.

2. Select another random r_i. Multiply upper y-axis boundary M and compare to $f(x_i)$, or $Mr_i \leq f(x_i)$. If this is true, the x_i is acceptable. If it is not, then repeat the process at step 1.

The efficiency of the rejection method relies on the ratio of the area of $f(x)$ to the boundaries of the axes. If the ratio is low, then the probability of rejection will be high, and if the ratio is high then the probability of rejection will be low. In a high probability of rejection regime, M might be relatively high or $f(x)$ might be a fine peak where the range of x-values under $f(x)$ is low compared to the x-axis boundary. Figure 14 provides an illustration of high versus low rejection probability; the graph on the left has a high probability while the graph on the right is low.

The rejection method utilizes the inverse method after it compares one PDF to another, $f(x)$ to $g(x)$, by finding the x value by $G^{-1}(r)$. As defined earlier, $F(x)$ limits are from $[a, x]$ up to the limit x_i. By use of the rejection method, $F(x)$ is defined in Equations 46 and 47.

$$F(x) = \int_a^x h(x')g(x')dx' \tag{46}$$

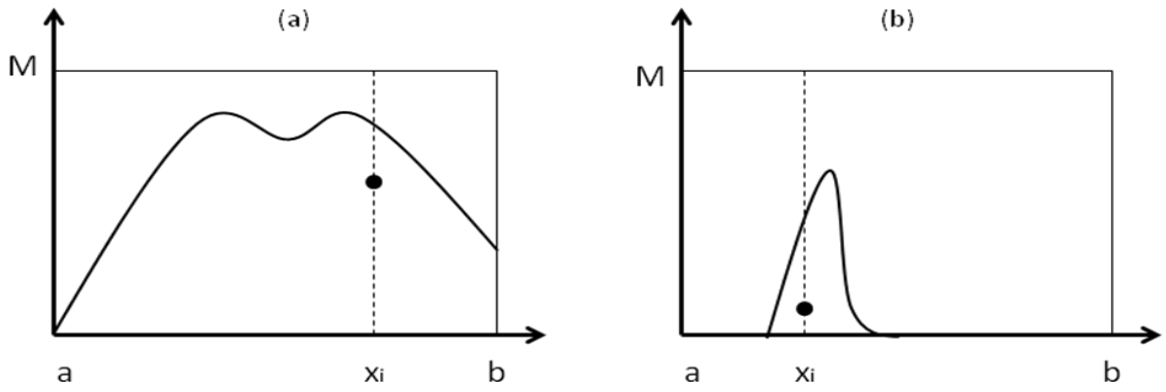

Figure 14. Rejection method examples of applications. (a) Depicts a low probability of rejection because the ratio of $f(x)'s$ area to the boundaries is high. (b) Depicts a high probability of rejection because the ratio of the $f(x)'s$ area to the boundaries is low.

$$h(x) \equiv \frac{f(x}{g(x)} \tag{47}$$

It is clear that when comparing one PDF to another that if $f(x)$ differs greatly from $g(x)$, then $h(x)$ will be low and vice versa. $h(x)$ must not exceed the defined h_{max} within $[a, b]$ by selecting a $g(x)$ that does not allow this. The rejection method takes on the following procedure.

1. Select a r_1.
2. Select temporary x by use of $x_i = G^{-1}(r_1)$.
3. Select a second r, r_2.
4. Reject x_t if $r_2 > h(x_i)/h_{max}$. Then return to step 1.
5. Accept x_t if $r_2 < h(x_i)/h_{max}$.

Figure 15 (a) shows a $f(x)$ and $g(x)$ that correlate to a $h(x)$ close to unity, whereas (b) shows a $h(x)$ that approaches 0 with a $f(x)$ differing more from $g(x)$.

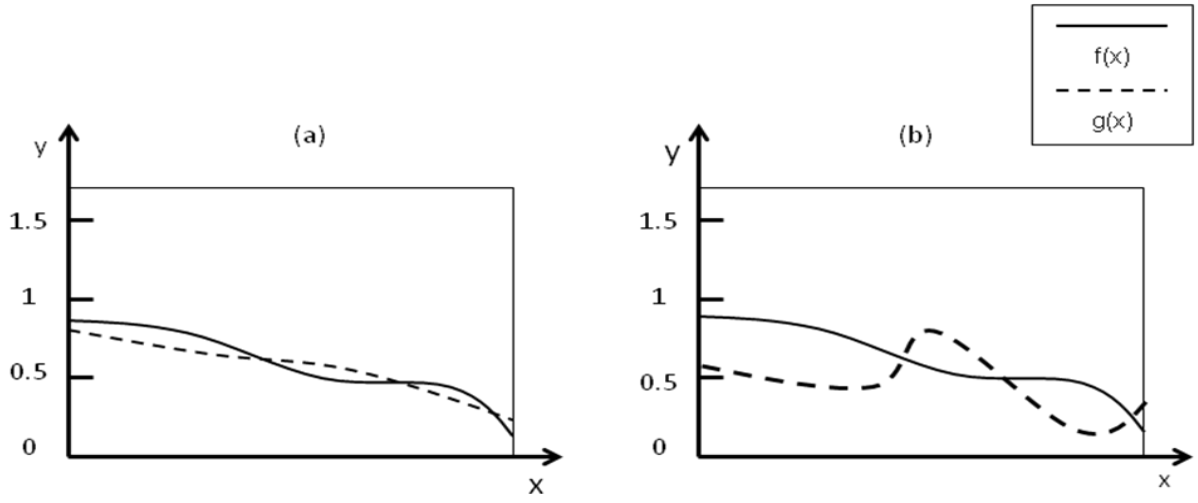

Figure 15. Rejection method examples of applications. (a) Shows a low deviating $f(x)$ to $g(x)$ plot where $h(x)$ is close to unity. (b) Shows a large gap between $f(x)$ and $g(x)$ so $h(x)$ approaches 0.

Scoring

PDF's are used to generate values x_i about the random variable x generated by pseudo methods mentioned earlier. A mean for all points produced per z are collected by scoring a large number N of histories of sample data given by Equation 48.

$$\langle z \rangle \equiv \int_a^b z(x) f(x) dx \simeq \frac{1}{N} \sum_{i=1}^{N} z(x_i) \tag{48}$$

For every history, the array must be initialized and then produces an array of $z(x_i)$. Then $\langle z \rangle$ is further estimated by $\langle z \rangle = S_1/N$.

An inherent flaw in Monte Carlo simulations is that when large numbers of histories are accumulated in a simulation, it is more difficult to reduce the standard deviation as shown in Equation 49.

$$s(\overline{z}) \propto 1/\sqrt{N-1} \simeq 1/\sqrt{N} \tag{49}$$

In Equation 49, the -1 under the root is removed due to a high N and the represents the sample mean, the standard deviation is halved when N reaches a multiple of four times. This high N is difficult to obtain and thus other methods must be used to solve this problem such as variation reduction techniques, which reduce the size of $\langle z \rangle$ described in the next section.

Not all random samples x_i can be contributed to the average of the population $\langle z \rangle$ because some samples are not important and do not contribute much to the mean. In other words if the simulation is supposed to produce a specific PDF such as a Watt spectrum, the simulation will produce a Watt spectrum but outliers may be inevitable in the system that show deviations in the data points that may affect the spectrum very much overall.

These data points are considered wastes of computation time and can be disregarded. The information they carry is not useful to the purpose of the experiment because they provide unnecessary data. Monte Carlo development has become very good at modeling by maximizing large numbers of high-weight and minimizing low-weight samples; this process is called biasing. The mean values with and without biasing will be different. By application of weights to scoring, important random samples will be given the weight value of $W_i = 1$, whereas less important samples x_i from $f(x)$ will be represented as a fraction such as a $W_i = 1/10$ or $1/100$, depending on how little importance the sample has. The use of biasing is described by Equation 50.

$$\overline{z} = \frac{1}{N} \sum_{i=1}^{N} W_i z(x_i) \tag{50}$$

Variance Reduction

As determined before, the Monte Carlo method utilizes a wide range of techniques to acquire appropriate samples and score them according to specific purposes of in-

dividual experiments. The beauty of Monte Carlo is that it is complex so that it can applied liberally and it is highly flexible. Because the error of this method is defined by σ^2/n, a simple solution to reduce the error would be to increase the number of samples n but this also increases the computational time. Another technique is to reduce σ by what is known as variance reduction. There are many variance reduction techniques but two are discussed here: importance sampling and splitting/rouletting.

When measuring a particular region, it is preferred that $f(x)$ approaches zero outside of the region. The problem is that the area of the region may be small or that the distribution falls close to the boundaries of the region, which makes the mean of the distribution distorted. Importance sampling values the importance of particular regions by placing a weight on them. The importance sampling estimate is expressed by Equation 51.

$$\langle z \rangle = \int_V \frac{z(x)f(x)}{f^*(x)} f^*(x)dx \equiv \int_V z^*(x)f^*(x)dx = \langle z^* \rangle \tag{51}$$

The weight importance function is $W(x) \equiv f(x)/f^*(x)$, so $z^*(x) = z(x)W(x)$. $\langle z \rangle$ and $\langle z^* \rangle$ are equivalent in Equation 52.

$$\langle z \rangle = \langle z^* \rangle \simeq \overline{z^*} = \frac{1}{N} \sum_{i=1}^{N} W_i(x_i)z(x_i) \tag{52}$$

A second type of variance reduction is called splitting and roulette and is used when particles transport through regions of different levels of importance. With splitting, a particle passing from a region of lower importance I_i to higher importance I_j is split into $n = I_i = I_j$ identical particles with weight $w = n$, so the particle's weight is cut in half while increasing the sampling number. The reverse is done when a particle transports from a higher importance region to a lower one; roulette is played and the particle does not exist anymore with a kill probability of $1 - (I_i = I_j)$ with

weight $w \times I_i = I_j$ [17]. Splitting and roulette balance each other because splitting increases computation time and decreases variance while roulette does the opposite. This balance results in a method of sampling from the most important regions.

3.3 Geant Monte Carlo Particle Transport

Geant is a Monte Carlo particle transport simulation and visualization software program that takes statistical distributions of particle transport through materials. It is used because it is impossible to rely on analytical calculations to predict neutron and other particle transport. Geant is a global leader in particle transport applications and provides a significant understanding of physics and detection capabilities. It implements a C++ coding environment to easily and efficiently manipulate the geometric environment, materials, and a variety of other parameters. Geant can simulate a variety of particles, including photons, hadrons, ions, and leptons, across a wide range of energies from thermal to the high energies (TeV) featured at the Large Hadron Collider at CERN. Its applications range from astrophysics, medical physics, materials science, high energy physics, etc [18].

The input deck in Geant is referred to as a kernel where many characteristics of a system are specified including the physical geometry, material types, physics applied to the system (i.e. electromagnetics, elastic scattering, etc.), detector response, graphics options, and others. Geant is object-oriented, meaning that the data structures are contained in objects. It operates on iterative implementations allowing the program to accept initial inputs and periodically update the objects during runtime [19]. Several Monte Carlo tools contain similar capabilities and interfaces to Geant such as MCNP and FLUKA.

Since the first production version in 1998, Geant has been continuously updated with geometrical, material, interaction, software, and performance enhancements.

Significant enhancements in the kernel include continuous monitoring of the runtime events and improved functionality. The software website provides a list of advancements and updates [20]. For the purpose of this research, the most updated version, Geant4.10.1, was used and the 2015 upgraded features in this version include two that are applicable to this research that include merging high precision neutrons with other particles for interaction reactions and "The development and validation of low-energy neutron elastic scattering [20]."

3.4 Response Function Optimization Approach

Analysis of HDPe thicknesses between detectors was done through Geant to detect the most neutrons and the most resolved response function over all detectors. The objective was to select HDPe widths thick enough that fast monoenergetic neutrons were thermalized for detection but thin enough so that the neutrons were not absorbed inside of or scattered outside the HDPe. The response function resolution of neutron counts per energy per detector had to be large enough to quantify and visualize specific neutron energies.

The optimization process began by selecting the first HDPe layer thickness; selection depends on source energy. A polyenergetic source that emits a large percentage of low energy neutrons found in many Watt spectra may require thinner initial HDPe layers because those neutrons are closer to thermal and may be absorbed or scattered by the HDPe if too much is used. Figure 16 shows relatively how many neutrons escape by scattering from HDPe. If the spectrum contains a large amount of high energy neutrons, on the other hand, thicker initial HDPe thicknesses are needed to significantly decrease the neutron energy to thermal for detection. Several response functions were plotted during the optimization process and are shown in Appendix A.

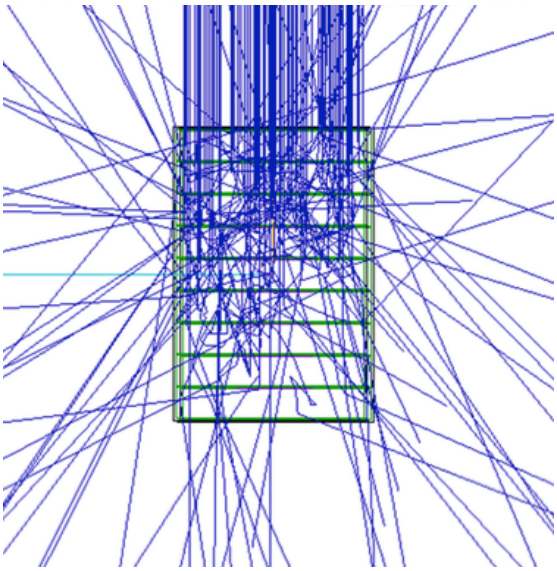

Figure 16. A Geant simulation was conducted using 100 neutrons interacting with the spectrometer to visualize how HDPe scatters neutrons. The Geant simulation also shows that neutrons are also absorbed by the HDPe and the detector, which is visually less obvious [21].

As a reference, 10 MeV neutrons were detected and produced a neutron count per detector. When the spectrometer it irradiated by 11 MeV neutrons, it produced a response similar to the 10 MeV neutrons, which makes it difficult to unfold these two neutrons. The HDPe thickness must be adjusted to separate the responses. Thinner HDPe layers allow better detection efficiency for slower neutrons. The HDPe layers were optimized depending on the monoenergetic neutrons' energies. The technique was verified with Monte Carlo and experimental techniques due to the probabilistic nature of neutron moderation and detection. The resolution of the response function determined if the polyenergetic neutron source could be unfolded. An example of a well-resolved response function is shown in Figure 17.

The legend represents the monoenergetic neutron irradiated through the spectrometer with layered moderators and detectors. The first number in the legend is the neutron energy, the next ten are the moderator thicknesses in centimeters, and

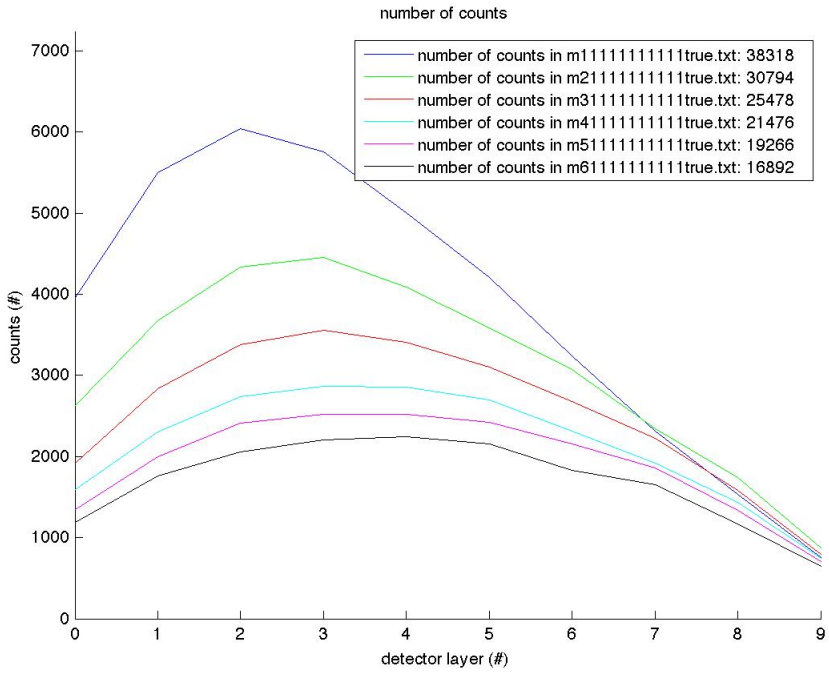

Figure 17. Example of a well-resolved response function.

the last number after the file name is the sum of neutrons detected per detector for each monoenergetic neutron. The respective counts per detector per energy group is located in Table 4.

Table 4. Example response function data

Detector Number	1	2	3	4	5	6	7	8	9	10
Energy (MeV)										
1.0	3951	5496	6048	5760	5007	4212	3238	2317	1532	757
2.0	2623	3673	4337	4452	4091	3589	3070	2345	1743	871
3.0	1916	2834	3379	3560	3411	3102	2674	2229	1582	791
4.0	1591	2302	2742	2868	2856	2702	2314	1919	1439	743
5.0	1342	1995	2411	2524	2516	2424	2152	1862	1339	701
6.0	1185	1762	2053	2206	2242	2153	1829	1650	1169	643

A thesis by Captain Michael Ford, an AFIT 2013 MS graduate, utilized Geant to perform D-D generator simulations on an LiF detector for similar neutron detection

purposes with success [21]. His results verified that those energies could be resolved. The unfolded neutron energies went up to 2.45 MeV, whereas this research unfolds energies up to 12 MeV, which are more difficult to resolve. After an optimized response function was developed, the source data was produced by insertion of a model PuBe source.

PuBe Neutron Source and Initial Guess

The polyenergetic source used in this research is a plutonium-beryllium (PuBe) neutron source, which produces a polyenergetic, mostly hard neutron spectrum. It contains mostly ^{239}Pu but has trace amounts of ^{241}Pu, which is a beta emitter and decays to ^{241}Am that also spontaneously emits alpha particles. The alpha particles from both the ^{239}Pu and ^{239}Am are converted to neutrons through the ^{9}Be(α, n)^{12}C reaction. The ^{241}Pu, however, can distort the energy signature of PuBe according to how much ^{241}Pu it contains [22]. The PuBe source used in this research is plotted in Figure 18 [23].

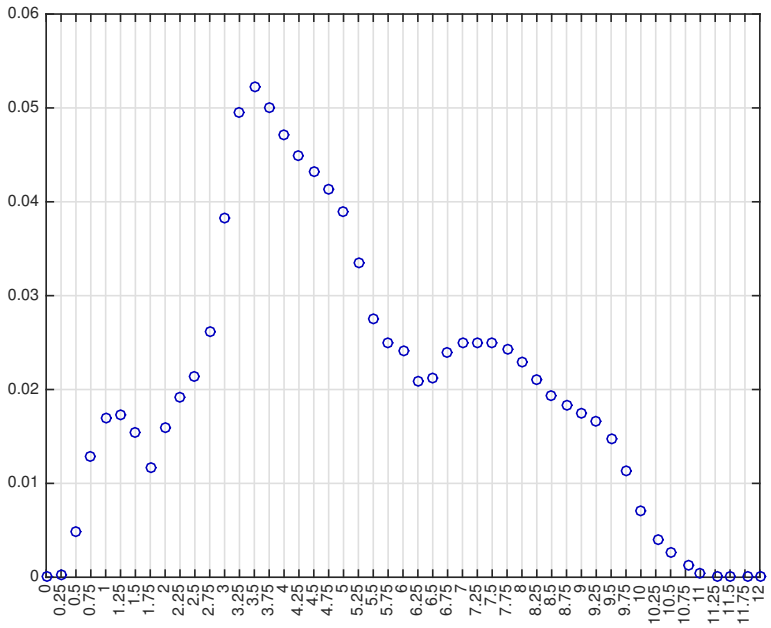

Figure 18. Specific PuBe source spectrum the MLEM method used [23].

The source data is a vector of the number of neutrons detected per detector via a polyenergetic source of neutrons irradiated through the spectrometer. All of the energy groups are smeared together, so each detector senses neutrons of all energies in a single response. Figure 19 shows the source data response of the polyenergetic PuBe response through the spectrometer.

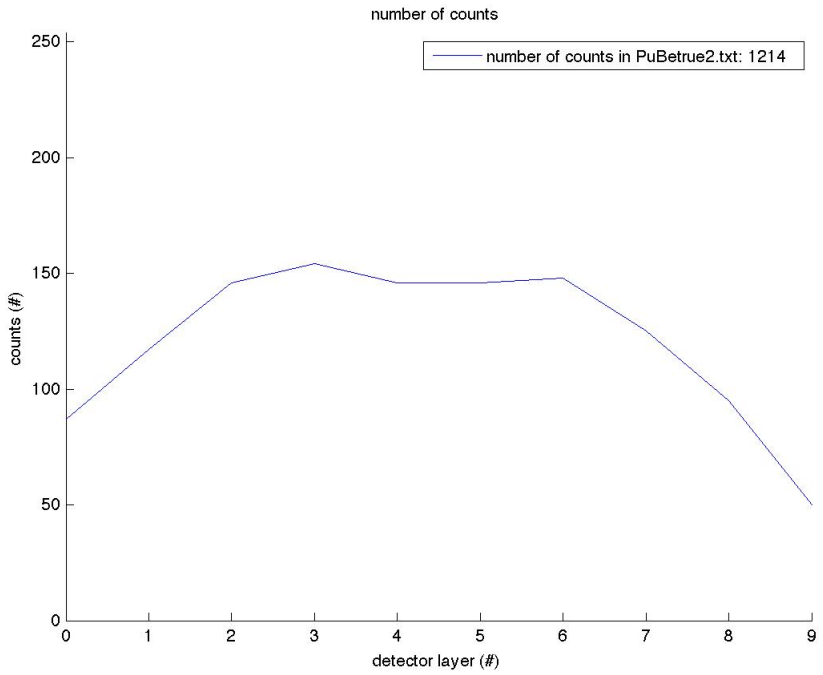

Figure 19. Polyenergetic PuBe spectrum through the [1111111111] thickness combination (numbers by centimeter)

The initial neutron spectrum guess must be any positive number ($\lambda > 0$). The final solution should closely resemble the source data intensity as close as possible due to the number of energy groups designated in the response function and how resolved those monoenergetic groups are from the Geant models. After all three steps have been collected by the Geant models, the spectrum can be unfolded. This is shown through the algorithm and the iteration convergence and termination techniques in the following section.

Spectrum Unfolding Algorithm, Convergence, and Example Result

Equation 27 was simplified to Equation 53 for ease of matrix operations and implemented in MATLAB 2015a, where variables are the matrices listed.

$$\begin{aligned} \lambda^{n+1} &= \frac{\lambda^n}{A} AN \frac{Y}{A\lambda^n} \\ &= \left\{ \lambda^n \left[A' \left(\frac{Y}{A\lambda^n} \right) \right] \right\} AN \end{aligned} \tag{53}$$

λ = initial neutron spectrum guess $\rightarrow$ matrix: energy bin by one.

A = response function $\rightarrow$ matrix: detector number by energy bin.

Y = source data $\rightarrow$ matrix: detector number by one.

N = coefficient with the value one for every element $\rightarrow$ matrix: energy bin versus detector number.

The process is calculated by matrix and element multiplication and division, where the dot before the multiplication or division sign represents elemental math. "Ones" represents a matrix of specified dimensions with elements equal to one:

$$\begin{gathered} A\lambda = (D \times E) \times (E \times 1) = (D \times 1) \\ Y./A\lambda = (D \times 1)./(D \times 1) = (D \times 1) \\ A'(Y./A\lambda) = (E \times D) \times (E \times 1) = (E \times 1) \\ AN = (E \times D). \times ones(D \times 1) = (E \times 1) \\ \{\lambda[A'(A\lambda)]\}AN = (E \times 1). \times (E \times 1) = (E \times 1) \end{gathered} \tag{54}$$

This algorithm produces an $(E \times 1)$ vector that is the solution spectrum.

MLEM performs matrix operations as described analytically above, and each iteration of the process results in a vector closer to the solution than the last, or rather the process converges to a solution. When the source data are normalized and the response function is not, the iterative spectrum solutions can be used to understand how the convergence is operating. For every iteration, $L(\lambda^n) < L(\lambda^{(n+1)})$, where L is the likelihood function and n is the iteration number, starting from the second iteration because the initial guess can be any value so long as elements of the guess are positive. This equation explains that the previous solution will always be less than the next solution until convergence. Table 5 shows the iteration sequence for the first ten iterations of an example process. Table 6 is the final solution.

Some elements in the solution vector increased and some decreased. The equation above indicates that the *sum* of the energy intensities increases after each iteration, and not the individual elements. The sum of the energy intensities have to increase and must be less than one because the source data counts were normalized; therefore, the solution converges [24]. Figures 20 and 21 plot the convergence of this example where the circle on the sum per iteration function pinpoints the location in the iteration process of the final solution. MLEM continues iterating until it is told to terminate. It terminates here after convergence is reached, and every sum per iteration thereafter contains the same intensities per element.

Table 5. Example MLEM first ten iterations

1.000	0.03563	0.03788	0.04005	0.04215	0.04416	0.04607	0.04788	0.04959	0.0512
1.000	0.03233	0.03139	0.03051	0.02969	0.02893	0.02823	0.02758	0.02698	0.02642
1.000	0.03321	0.03304	0.03285	0.03264	0.03241	0.03217	0.03192	0.03167	0.03142
1.000	0.03305	0.03277	0.0325	0.03225	0.03201	0.03179	0.03158	0.0314	0.03123

Table 6. Example MLEM final iteration

0.07074
0.01808
0.02185
0.03813

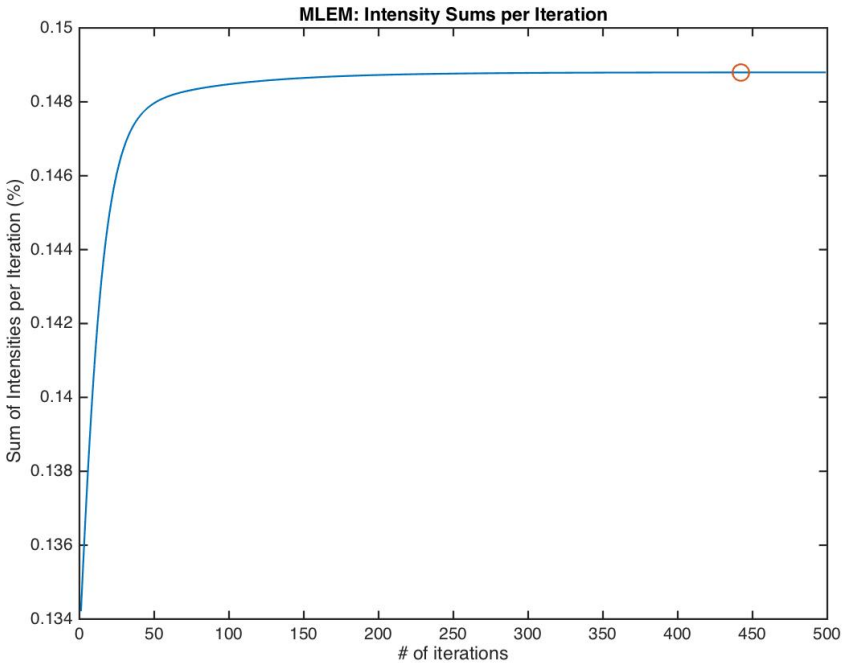

Figure 20. Example non-normalized linear MLEM unfolded solution with the circular point that indicates the final unfolded solution; intensity sums were equivalent to the termination point at every iteration thereafter.

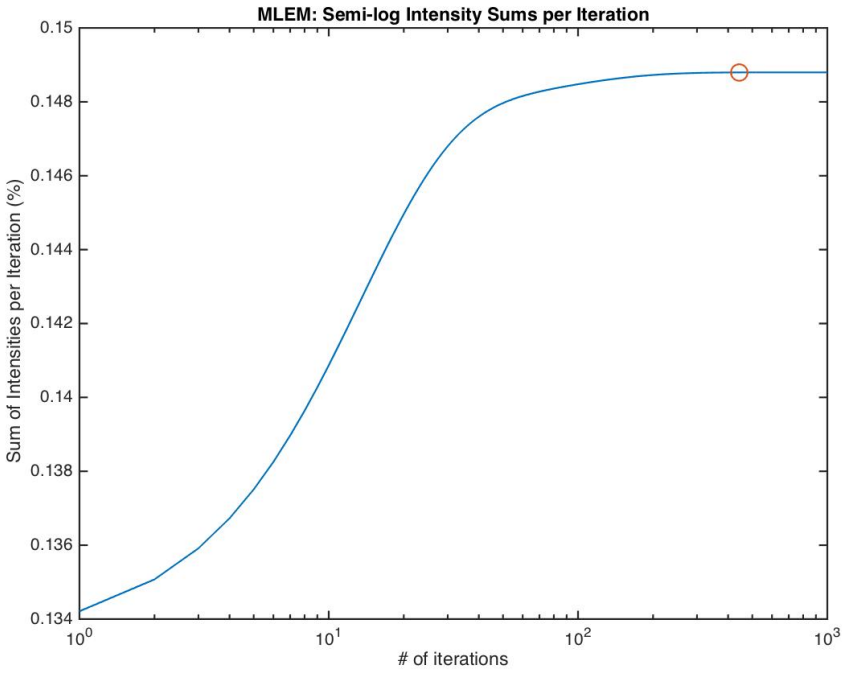

Figure 21. Example non-normalized semilog MLEM unfolded solution with the circular point that indicates the final unfolded solution; intensity sums were equivalent to the termination point at every iteration thereafter.

3.5 Experiment

Since the detector is an efficient thermal neutron detector, neutrons above 0.025 eV must be moderated to be detected. This experiment used a fast neutron PuBe source so the neutrons were moderated with an efficient moderating material that quickly slowed the neutrons to thermal. Hydrogenous materials make great moderators because hydrogen is one of the best moderating elements due to its high scattering cross section coupled with its low nuclear mass to transfer a large portion of its energy for detection. Specifically, HDPe (CH_2) was used to moderate the neutrons. The setup of the detector and HDPe is shown in Figure 22. The power supply and preamplifier in this figure as well as other electronics in detection process are discussed in the following sections of this chapter.

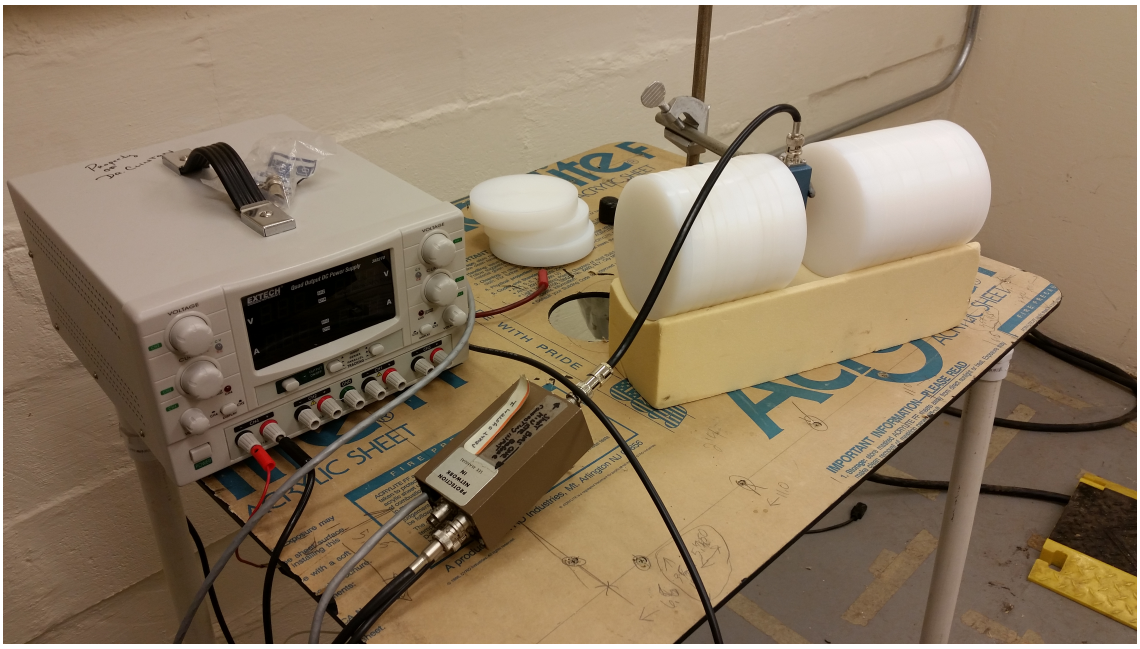

Figure 22. Spectrometer setup with power supply and preamplifier.

Certain thicknesses of HDPe are optimal to moderate certain neutron energies to thermal. Geant modeled the thicknesses to moderate monoenergetic neutrons and those from a PuBe polyenergetic source. More moderating material is ideal to slow

higher energy neutrons, yet moderators that are too thick may either scatter more neutrons out of the spectrometer or absorb them before reaching the detector, so fewer neutrons will be detected; more neutrons over the same time period produces a better signal to be able to create a more accurate energy spectrum. The HDPe was optimized through Geant because particle transport involving absorption and scattering is highly probabilistic and particle statistics must be utilized to analyze the distribution functions for these experiments. The detector was placed 0.5 m away from the PuBe source. The first neutron count history recording was collected by placing a 1.0 cm HDPe disc in front of the detector. Due to the limitation of having only one detector for the experiment, an addition of a 1.0 cm HDPe disc was placed in front of the detector after every count history was recorded until 30.0 cm HDPe was placed in front of the detector. The benefit of using only one detector was that there was no operational variation between multiple detectors. After the tests were completed, select HDPe thicknesses were chosen according to the optimization combinations produced by Geant model for the analysis.

Equipment

The spectrometer was characterized with the equipment in Table 7, the configuration diagram for the electronics is shown in Figure 23, and the following sections describe the equipment used.

Preamplifier and Shaping Amplifier

A power supply applies a voltage in order to produce a current from the reaction products, which is proportional to their deposited energy. This is fed into a fast preamplifier. The preamplifier was used because total charge immediately produced by the conversion reaction is usually too small to measure accurately, and it also re-

Table 7. Lab Equipment Used in the Present Research

Solid-state thermal neutron detector
PuBe source
High density polyethylene discs
Ludlum Measurements Inc., Count Ratemeter, Model 12-4
Extech Quad Output DC Power Supply, Model 382270
Ortec EG&G Preamplifier, Model 142IH
Ortec Spectroscopy Amplifier, Model 672
Ortec Timing SCA, Model 551
Ortec Timer/Counter, Model 996
Ortec ADCAM MCB, Model 926
BK Precision Function Generator, Model 4078
LeCroy WaveRunner Oscilloscope, Model LT58M
GammaVision software

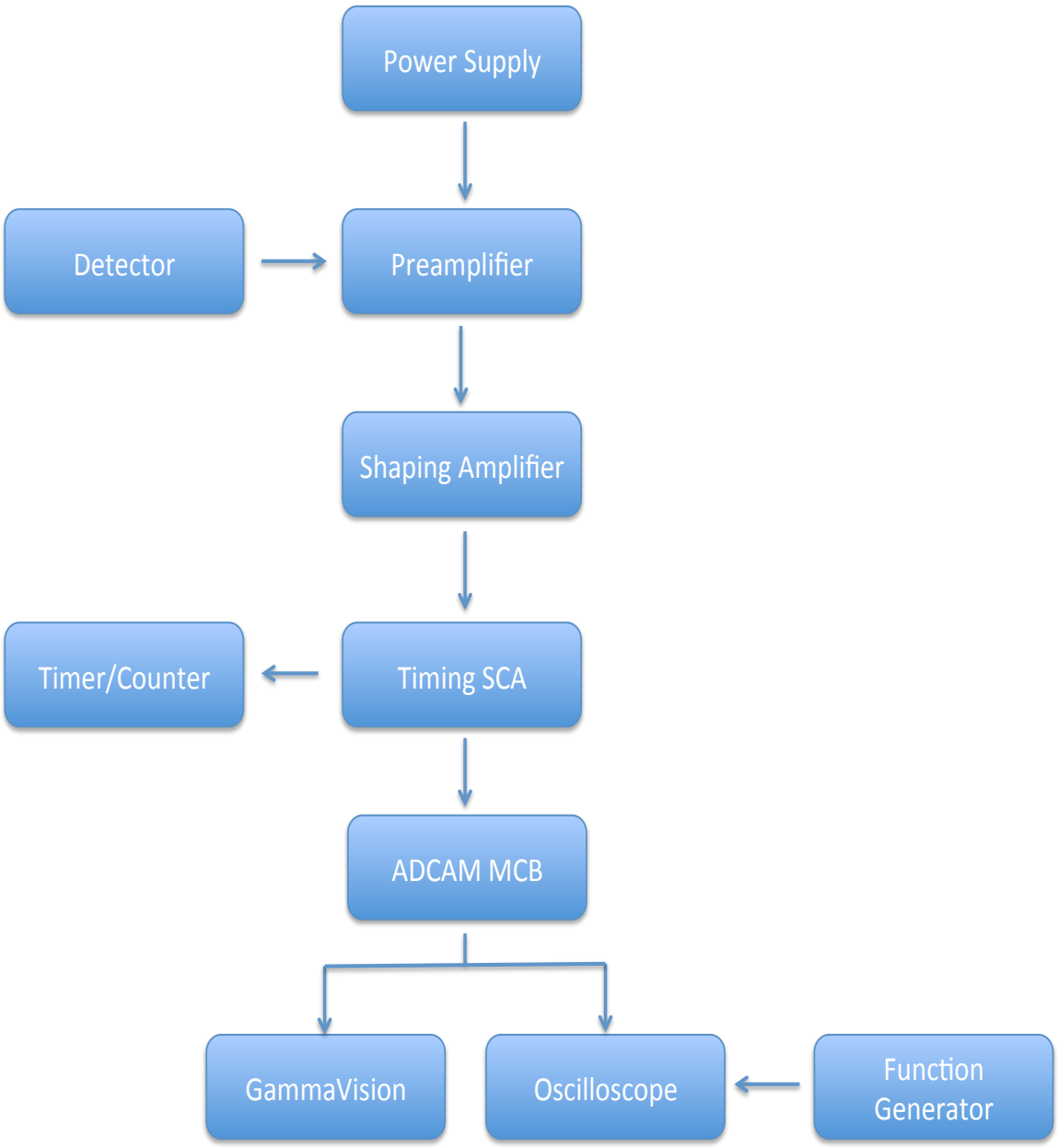

Figure 23. Electronic configuration for the spectrometer experiment.

duces noise and interference before further electronic analysis. The shaping amplifier converted the electronic signal from the preamplifier to a signal pulse that the system could translate because the signal from the preamplifier was not large enough to be interpreted. Amplifiers prevent pulse overlap because they can quickly return pulses to the baseline, which increases signal-to-noise ratio; however, there is always a likelihood that two pulses can overlap due to high particle interaction rates that may alter the output signal. This may result in pulse "pile-up." The shaping amplifier passed the output voltage signals to additional electronic circuits.

Timing SCA, ADCAM MCB, and Timer/Counter

The timing single-channel analyzer (SCA) read the signal from the shaping amplifier. Through the single-channel pulse-height capability, the timing SCA was able to discriminate against the background and electronic noise to capture only the specified conversion particle currents from the neutron events with the use of the lower level discriminator. Timing SCA's also have an upper level limit but it was not necessary for this experiment because the importance was placed on collecting energies above a particular limit [25]. The timer/counter counted the events that took place over a certain time period, which served as a verification that the neutrons were being recorded by the system. The ratemeter also served as verification by counting the events in a similar manner.

A multichannel analyzer, ADCAM, separates the pulses by height for each event, or interaction. Each height bin is assigned to a range of channels. The result is a histogram of bins where each bar is the number of pulses contained within certain pulses (energies). This is called the pulse height spectrum. The spectrum contains digital values that can be interpreted by a programming software for analysis. Timer/counter components were utilized to verify that neutrons were being recorded by the system

after having specified a lower pulse bound that produces a total pulse count [7]. The amplifier, timing SCA, ADCAM, and timer/counter are shown in Figure 24.

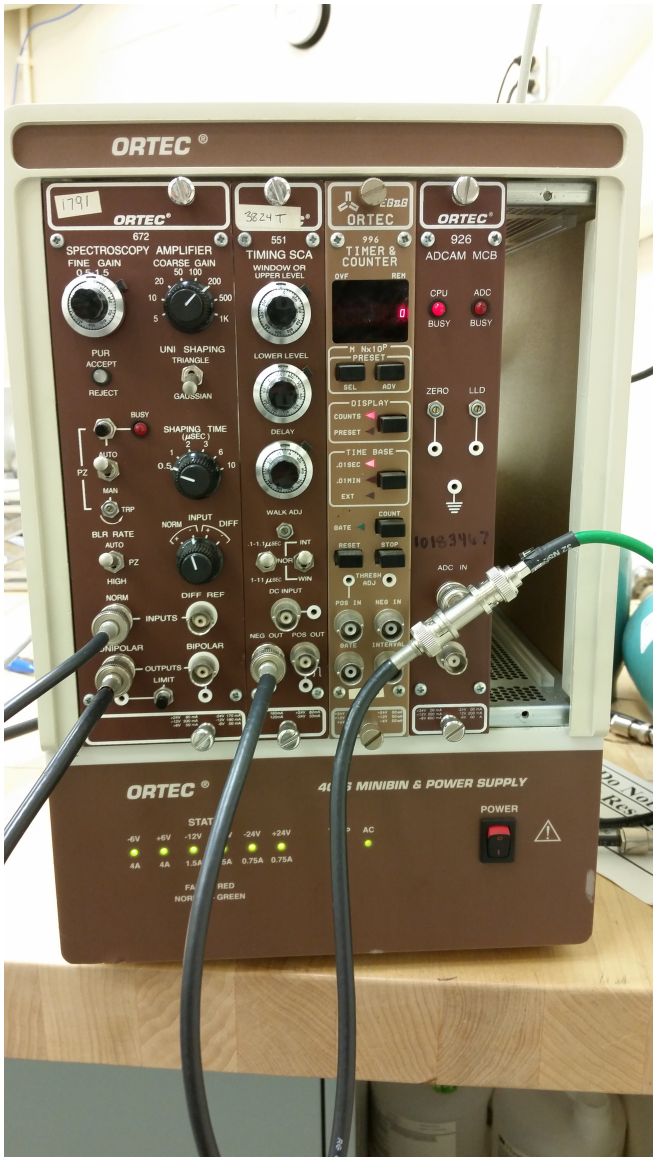

Figure 24. Electronic configuration for the spectrometer experiment.

Function Generator, Oscilloscope, GammaVision

Function generators take a current from an input signal, calculate the voltage, and translate the voltage over a specified time interval into a specific shape. The shapes

can be triangle, square, or sine. They can also limit input to certain wave frequencies and amplitudes [26]. The function generator in this research was used to interpret pulses from a neutron detector that converts thermal neutrons from neutron capture into two charged reaction products. The function generator fed an oscilloscope where the voltage was visualized as a verification that neutrons were present. Both the function generator and the oscilloscope are shown in Figure 25. Data collection and analysis was performed using by GammaVision [27].

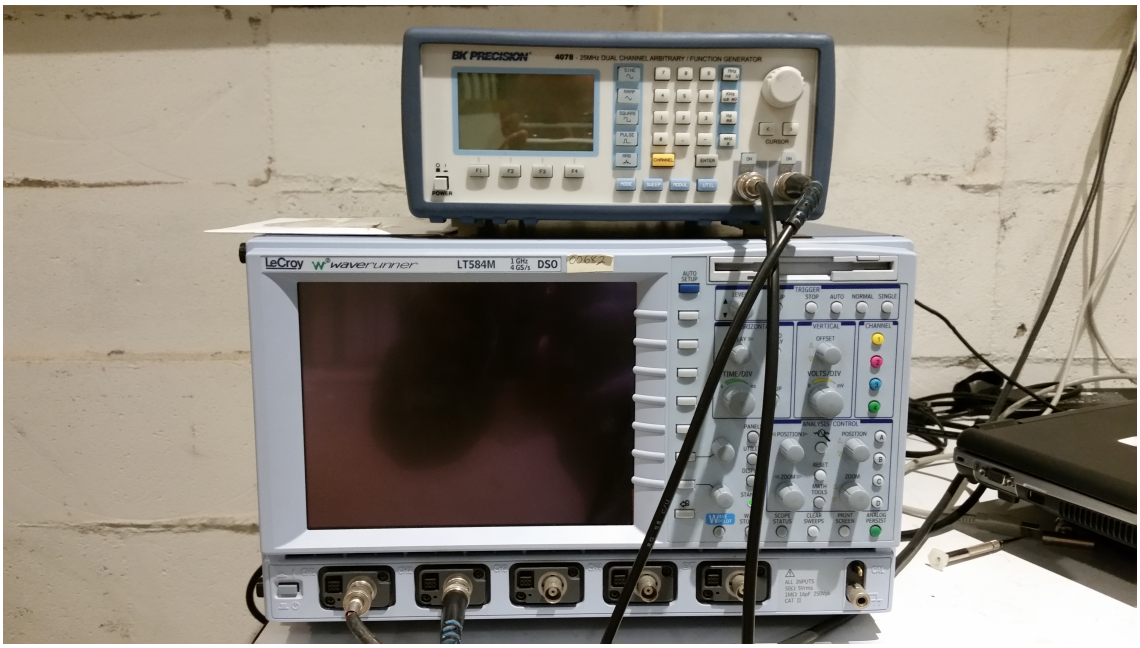

Figure 25. Function generator and Oscilloscope

GammaVision is a spectroscopy analysis software written initially for both high and low resolution gamma spectroscopy; however, photons are not the only particles that can be analyzed with this software. It uses an intuitive interface that accurately measures attributes of input spectra for data analysis. GammaVision provides a function for many applications including power plants, research, production labs, monitoring systems, and others [27].

The ADCAM transferred the digital output signal to GammaVision where it read the signal and produced a spectrum of neutron pulses. The detector only converted thermal neutrons but produced currents from both alpha and lithium-7, so the spectrum contained events over a range of channels as opposed to one. GammaVision records dead time and real time. The real time was collected for analysis to determine when the number of events was statistically significant with a counting error of less than 5%. This was used to record histories with a different thickness of moderator in front of the detector. Counts of 1000 events gave a counting error of 3.16% by Equation 55. Figure 26 displays the GammaVision interface. The following section describes the finer details of how currents from the reaction products are collected.

$$\text{counting error} = \sqrt{\text{count}}/\text{count} \tag{55}$$

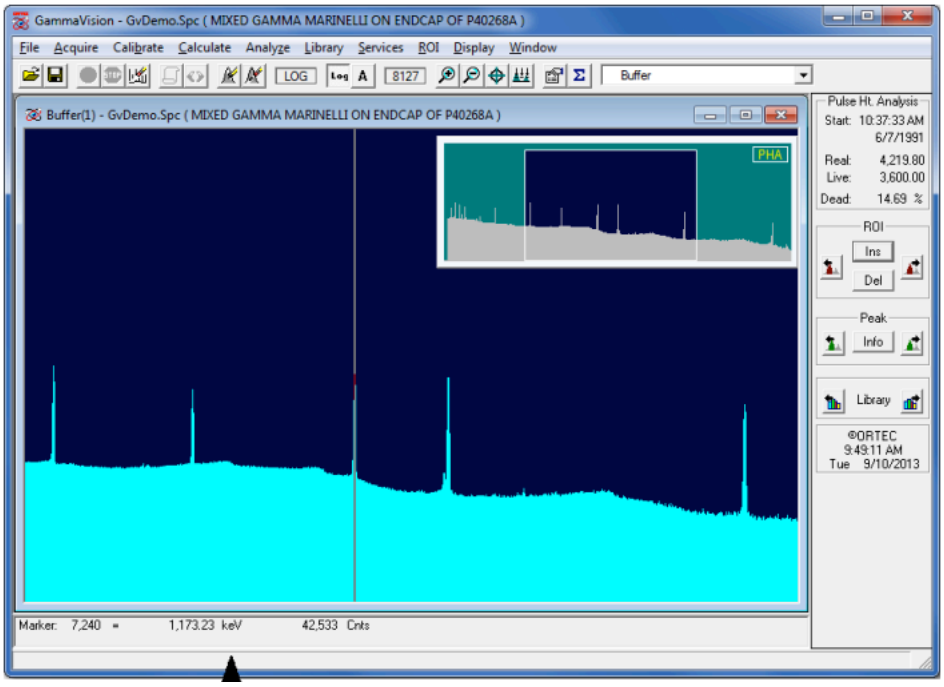

Figure 26. GammaVision interface that shows an energy spectrum [28].

Charge Carrier Detection

The neutron detector is a solid state detector that utilizes semiconductor physics to capture voltage signals in the multichannel analyzer. The detector captures thermal neutrons with a 22.5% efficiency, and it contains a 99% weighted ^{10}B conversion material that converts neutrons to alpha particles and lithium-7 atoms by the ^{10}B(n, α)^{7}Li reaction. The products ionize lattice atoms along their ionization tracks to create electron-hole pairs. A voltage was applied to the detector so the charge carriers drifted toward an electrical contact at the boundaries, where the resulting voltage created a measurable pulse.

Charge carriers do not have equal mobilities in the lattice, so charge collection times were different shown in Figure 27 (top). The resulting induced charge increased with the number of charge carriers collected at each electrode with respect to time, as shown in Figure 27 (bottom). Semiconductors rely on the total charge collection from both electrons and holes because the hole mobility in semiconductors is lower than electron mobility by a factor of two or three [7]. Carrier 2 travels for a longer time period before reaching the electrode. The collected charges produce an increased induced charge at the electrodes with increasing time. The last charge carrier to the electrode completes the total induced charge (bottom). The neutrons that are absorbed by the detector follow these charge carrier functions, but it is also important to know what happens to the neutrons that scatter away from the spectrometer and the ones that do not interact with the spectrometer as well.

Special Considerations

The PuBe source was located in a restricted area of AFIT and was surrounded by thick, high density concrete for safety purposes. The concrete was layered by material that can absorb and scatter high energy neutrons. Concrete can contain different

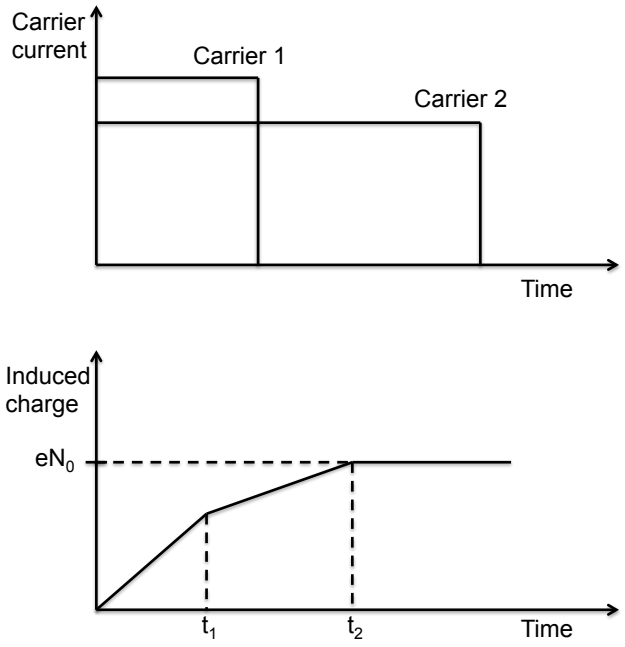

Figure 27. Carrier current with respect to time with two charge carriers. The carrier mobility leads to different accumulated currents (top), which affects the arrival times (bottom).

materials. The concrete at AFIT was layered so that concrete with higher scattering cross section was closer to the neutron source, whereas concrete with higher absorption cross section materials was further from the neutron source so that the neutrons were moderated and absorbed to avoid passing through the concrete. From a MCNP model performed by Okuno et al. [29], polyethylene had better moderating performance than concrete for a D-D neutron source after approximately 80.0 cm shown in Figure 28. The significance is that while concrete is a great shield for neutrons depending on material, the polyethylene moderator used for the spectrometer experiment is a great tool because of its hydrogenous makeup which makes for efficient moderating characteristics. The concrete used in the Okuno experiment contains hydrogen in the form of H_2O in the peridotite concrete but not with the same abundance as polyethylene. The concrete at AFIT performs well, which was also verified by the counts collected by the ratemeter outside of the concrete walls.

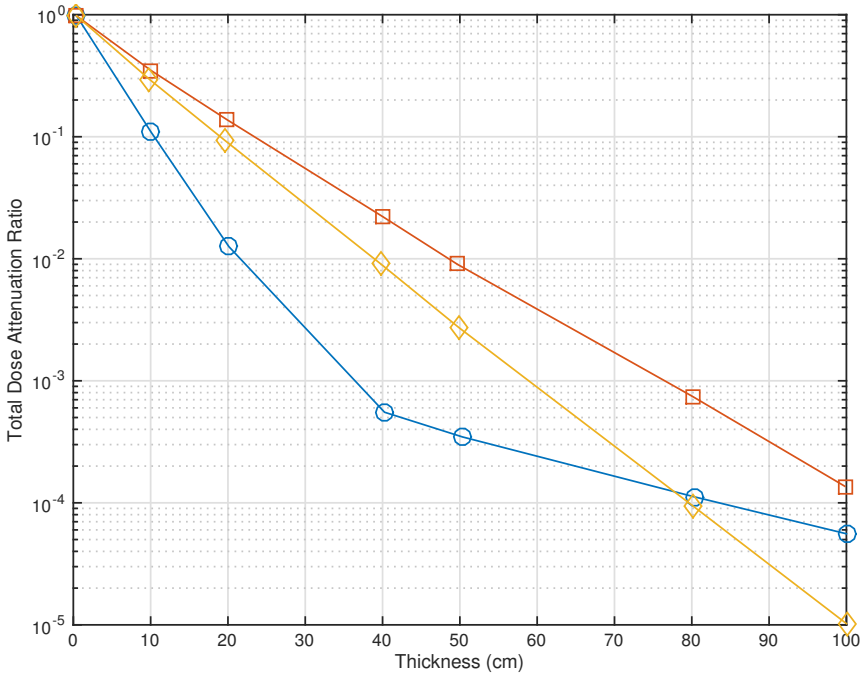

Figure 28. Comparison of moderating characteristics of polyethylene and neutron shield concrete.

4. Results and Analysis

The intent of this research is to identify the spectrum from a known or unknown radioactive source by the MLEM method. The Geant particle transport code was used to simulate monoenergetic neutrons in a spectrometer with layers of HDPe to produce a response function matrix. An optimal response function was selected and the efficiency of the spectrometer was analyzed. A parameter study of the effect of the square size of the detector on efficiency was then performed.

The optimized spectrometer was irradiated with a polyenergetic PuBe neutron source, and a response function was produced. The MLEM method was then performed on the information from the monoenergetic and polyenergetic neutrons in order to unfold the neutron source into an array of energy intensities. To prove that MLEM worked, the source response function was replaced by individual monoenergetic neutron energies. The experimental source data collected was provided by an actual PuBe source and unfolded by MLEM. The model and experimental unfolded solutions were compared via their difference ratios and variances from unity. Finally, the model and experiment solutions were compared to reference spectra provided by non-AFIT affiliates.

4.1 Response Function

Geant was used to produce the response function shown in Figure 29 with a HDPe thickness of 1.0 cm through all layers. Energy bins of [0.5, 1.0, 1.5, 2.0, 2.5, 3.0, 3.5, 4.0, 4.5, 5.0, 5.5, 6.0, 7.0, 8.0, 9.0, 10.0, 11.0, 12.0] were used to obtain the final solution to the unfolded neutron spectrum. Ten million monoenergetic neutrons of each energy bombarded the spectrometer to obtain a response function that was statistically significant, or without much count variation between tests.

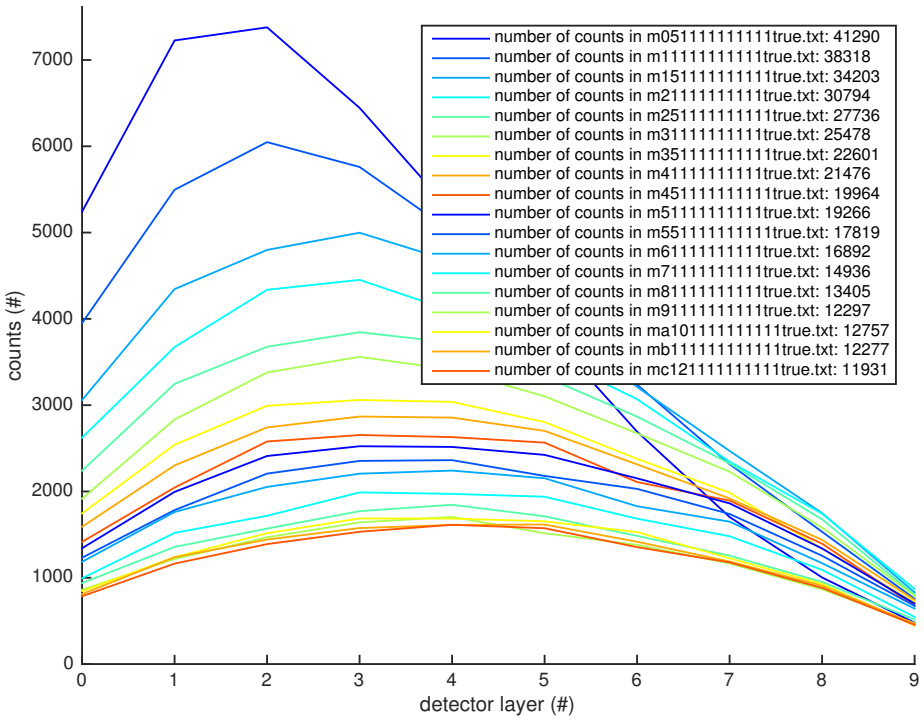

Figure 29. Number of neutrons detected per detector layer

As expected, the spectrum was more readily resolved for lower energies because it took less HDPe to moderate them. With increased HDPe for higher energy neutrons, the moderation became more probabilistic, so higher energy neutrons could not be resolved as easily. Lower energy neutrons were more abundant in the response function because those neutrons were already closer to thermal energy, so it did not take many collisions within the HDPe to moderate them. Higher energy neutron count peaks had lower values and were shifted to a deeper detection layer due to the number of collisions required. Each monoenergetic neutron had a maximum neutron absorption peak, and the number detected after that detection layer decreased consistently until the last detector.

Detection Efficiency

There are three processes governed neutron transport in the spectrometer: loss by scattering out of the HDPe, loss by absorption of the HDPe, and absorption by the detector conversion material. Loss by scattering out severely reduced the efficiency of the spectrometer due to the larger cross section and thickness of the HDPe layers as compared to the smaller detector. Ten million neutrons bombarded the spectrometer, but $< 0.45\%$ of them were detected. Figures 30 and 31 show the measured efficiency of the spectrometer. Figure 30 displays the total fraction of the sum of the counts of each monoenergetic neutron detected by every detector in the spectrometer. Figure 31, on the other hand, shows the fraction of the counts of each monoenergetic neutron at every detector in the spectrometer.

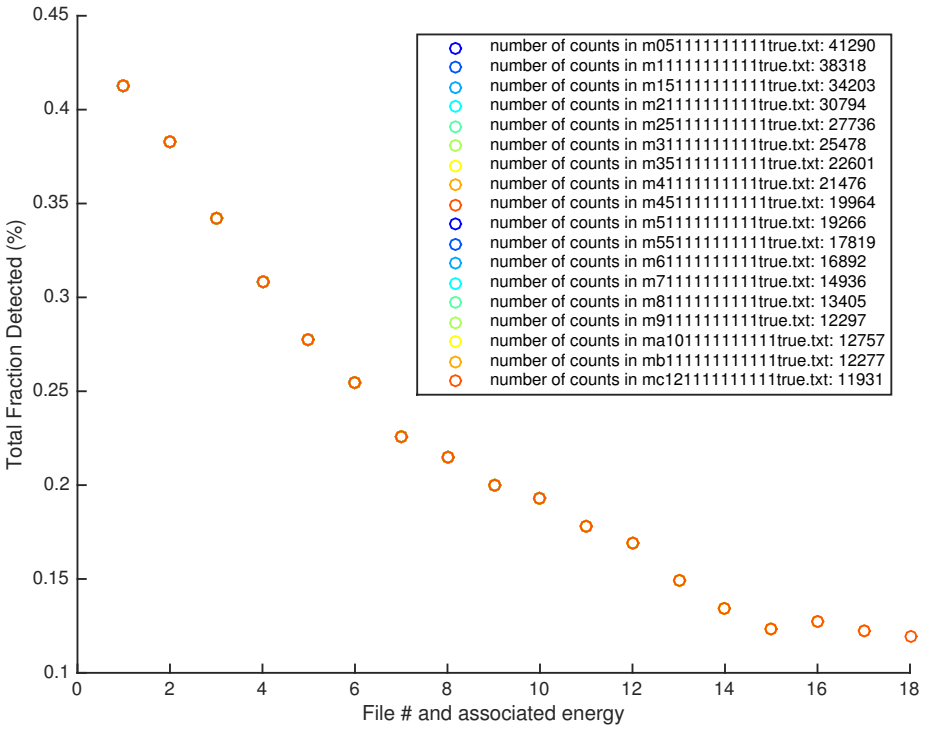

Figure 30. Total fraction detected vs. monoenergetic neutron source count

The total monoenergetic neutron fraction detected was between 0.1% and 0.45%. In reality, each detector is only 45 µm thick and has a 2.5 cm^2 area. A parameter

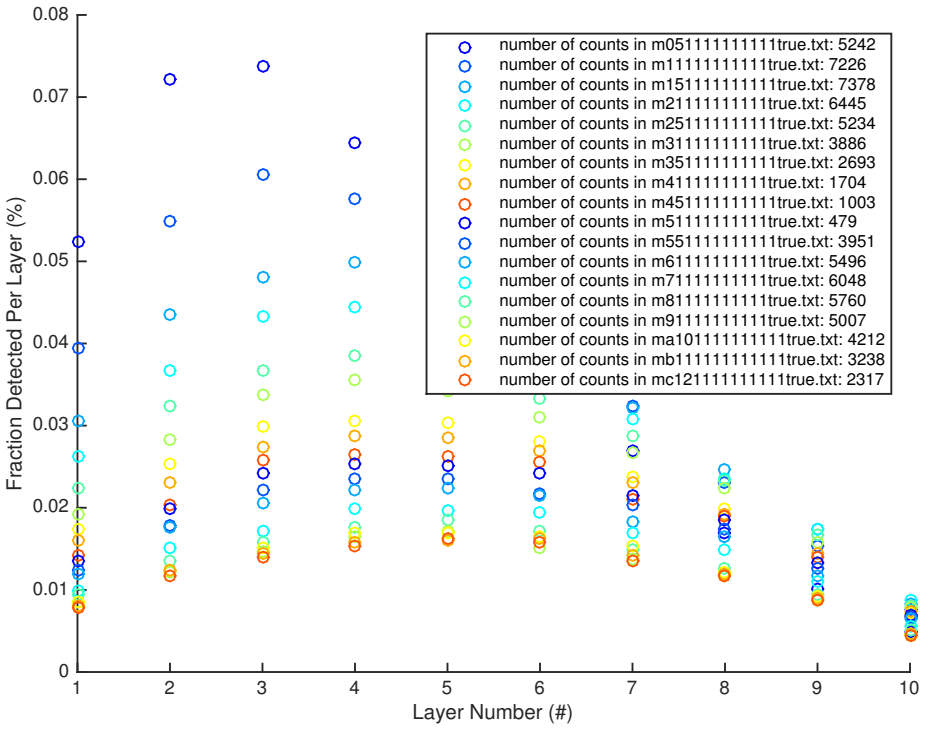

Figure 31. Fraction detected per detection layer vs. monoenergetic neutron source count

study was conducted on the areal size of the detector to see how the size affected the efficiency, and whether an increase in the size would produce better results. The detector thickness was not considered because multiple collisions could take place within the detector, which would skew the results. Table 8 shows the effect of areal size on efficiency. The parameter study demonstrated that the areal size had a large impact on the efficiency of the spectrometer.

Table 8. Detection efficiency per monoenergetic neutron per detector.

Area (cm^2)	6.25	25.0	100.0	10000.0
Efficiency (%)	0.84	3.35	13.39	87.86

Source Data

The response function was optimized with a 1.0 cm HDPe thickness combination. Then a polyenergetic PuBe source, shown in Figure 18, irradiated the spectrometer with this thickness combination for the MLEM unfolding method. The spectrometer was irradiated by the source shown in Figure 19. There is only one response line because all of the polyenergetic neutrons bombarded the spectrometer at the same time, so the line is a 'smear' of all of the neutron energies summed together. The most probable neutron energy of PuBe is located at approximately 3.5 MeV, and the average is located around 5.0 MeV. The goal of this research is to produce a spectrum that replicates the PuBe spectrum.

4.2 MLEM

MLEM was paramount to the success of this research because it was an efficient mathematical iterative reconstruction process that did not require an estimated initial

guess to unfold the solution. As long as the initial guess was greater than zero, the MLEM method performed as expected to unfold the spectrum.

Using the response functions modeled by Geant and the spectrum from the PuBe source, MLEM was able to unfold the spectra. Every iteration of the MLEM process produced an energy intensity vector whose sum was equal to 1.0 when both the source and response functions were normalized.

The solution converges and the sum of the intensities per iteration increases by $\lambda^{(n)} < \lambda^{(n+1)}$ when the response function is not normalized, as shown by the linear and semilog plots in Figures 32 and 33, respectively. The iterative process did not have a defined termination point, so the unfolding routine termination was subjective. A specific termination point could be selected, or it could be terminated when the solution spectrum looked most similar to the reference spectrum. The results shown in this research used the specified termination point method. A lower limit was selected such that any element in the solution vector with a value less than 10^{-4} terminated the routine; the solution at that point is the solution as deemed statistically appropriate. The red circles on the plots are those termination points.

MLEM Proof

The solutions in Figures 32 and 33 are functionally correct, but it was important to quantify them to make sure MLEM was unfolding the spectra exactly the way it was supposed to. The quantification in Tables 9 through 13 help to describe how MLEM solve the spectra. MLEM produced valid spectra solutions. As proof, monoenergetic neutron responses were substituted into the source data vector Y. The result showed the weight of the monoenergetic neutron in the solution vector λ.

The tables were organized by the monoenergetic neutron response input through Geant in the first row. The iteration numbers were placed in the second row, where

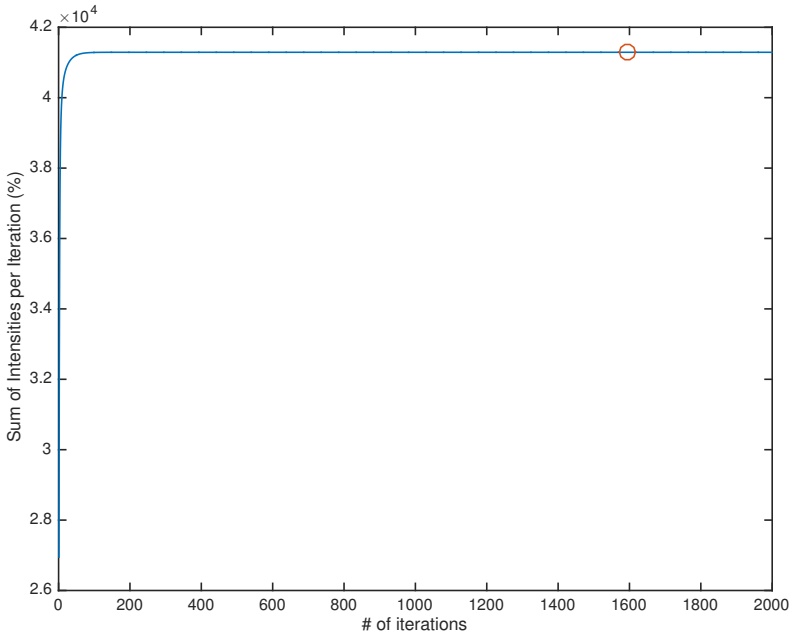

Figure 32. Linear plot of the converging iterative MLEM solution.

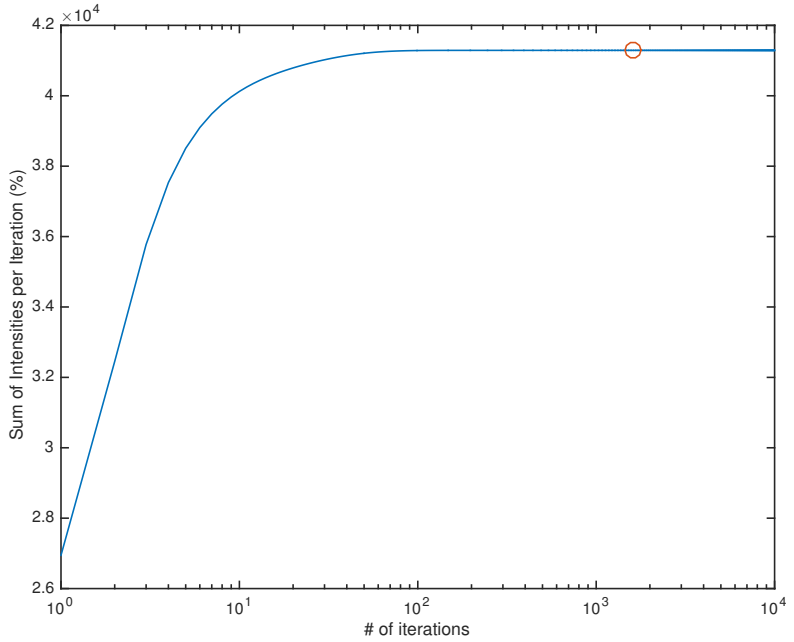

Figure 33. Semilog plot of the converging iterative MLEM solution.

the iterations were selected by orders of ten up to the termination limit. The third and following rows were the unfolded solutions for each specified energy used in the 1.0 cm thickness combination by specified iteration. Only certain monoenergetic neutrons were selected for this proof to show that several monoenergetic neutrons from different points in the array of energies could be successfully unfolded according to their resolution in the response function.

A larger sample of higher energy neutrons were selected because those were the more difficult energies to unfold, as they were less resolved in the response function. All selected monoenergetic neutron termination points were set to the point at which those neutrons reached 70% of their fully unfolded 100%. It was determined that 70% was good enough to show that the MLEM method was working the way it should. As the percentage increased, the number of iterations became so large that the concept of the number of iterations lost significance. The 0.5 MeV neutron was the only neutron in the sample energies to use 90% because the lowest energies were the most easily resolved; therefore, the number of iterations was low enough that significance was not lost.

The tables confirm that the monoenergetic neutron response function could be unfolded by the MLEM method. The intensity for the monoenergetic neutron approaches 100%. Some energies were more difficult to unfold because of:

Some energies were more difficult to unfold than others. Some required a large number of iterations to reach a specified termination point; therefore, for the 0.5 MeV neutrons the termination point was set to 90% and the 70% for all others. For some, the ratio was between the unfolded neutron's termination point (last element of the row in yellow) and the next closest neutron's intensity (cell in red in the termination solution) was small. A smaller ratio meant that it was more difficult to resolve. The ratio is calculated by Equation 56.

Table 9. 0.5 MeV MLEM

0.5 MeV			
Iteration	10	100	terminal (127)
Energy (MeV)			
0.5	0.186777288	0.875239087	0.900498124
1.0	0.104865872	0.07560315	0.064740865
1.5	0.072563816	0.016282613	0.012457199
2.0	0.063425985	0.009003044	0.006577244
2.5	0.055075288	0.004979631	0.003483818
3.0	0.049933671	0.003353833	0.002281412
3.5	0.050664437	0.00356213	0.002434423
4.0	0.044345457	0.002003103	0.00131008
4.5	0.041370199	0.001509421	0.000967437
5.0	0.039302955	0.001205533	0.000759581
5.5	0.037732627	0.001018012	0.000633537
6.0	0.038863311	0.001144778	0.000718289
7.0	0.035596745	0.000813654	0.000498922
8.0	0.037660251	0.001026217	0.000639731
9.0	0.037672046	0.001028895	0.000641568
10.0	0.03404914	0.000682802	0.000413646
11.0	0.034912651	0.000746992	0.000455018
12.0	0.035188261	0.000797106	0.000489107

Table 10. 3.0 MeV MLEM

3.0 MeV

Iteration	10	100	1000	10000	terminal (36369)
Energy (MeV)					
0.5	0.055766919	0.056123595	0.045536589	0.004569924	5.93E-05
1.0	0.055775901	0.057024545	0.060522406	0.045816696	0.008824784
1.5	0.055713175	0.056812128	0.063185409	0.074795187	0.032697072
2.0	0.055698469	0.056821858	0.065175531	0.10277107	0.059234832
2.5	0.055612511	0.056048108	0.058818893	0.055045205	0.021045094
3.0	0.055690201	0.057035208	0.071252088	0.265660859	0.700003289
3.5	0.055604796	0.056066646	0.060071961	0.069710521	0.037633553
4.0	0.055496417	0.055040425	0.051521526	0.022087102	0.00284964
4.5	0.055568508	0.055913163	0.060968168	0.084245626	0.047887084
5.0	0.05549638	0.055185903	0.054304294	0.039600362	0.01281511
5.5	0.055509219	0.055374055	0.05660569	0.055956317	0.027719971
6.0	0.055422346	0.05439934	0.047405443	0.015743509	0.002229574
7.0	0.055456586	0.054869485	0.0523514	0.031734952	0.009971501
8.0	0.055396425	0.054154414	0.045486933	0.009875445	0.000677451
9.0	0.055471426	0.054962847	0.052579504	0.030295063	0.007477678
10.0	0.055409302	0.054408671	0.048552556	0.016437539	0.001885893
11.0	0.055383605	0.054104404	0.045742015	0.010319379	0.000693043
12.0	0.055527814	0.055655206	0.059919594	0.065335242	0.026295149

Table 11. 7.0 MeV MLEM

7.0 MeV

Iteration	10	100	1000	10000	terminal (14104)
Energy (MeV)					
0.5	0.039562402	0.004105679	1.12E-06	7.91E-12	2.93E-12
1.0	0.046070426	0.01227033	7.55E-05	2.54E-08	1.12E-08
1.5	0.05056641	0.024208651	0.001175487	1.26E-05	8.16E-06
2.0	0.052118668	0.029808916	0.002259671	1.62E-05	8.23E-06
2.5	0.054020127	0.038930586	0.0072041	0.000397698	0.000277738
3.0	0.055200493	0.045403845	0.012614201	0.000976962	0.000667111
3.5	0.054994469	0.044075545	0.010660785	0.000405674	0.000230438
4.0	0.056724868	0.055148015	0.025352692	0.002092812	0.001221158
4.5	0.05762517	0.061829654	0.040264069	0.006655622	0.004285606
5.0	0.058322733	0.067496759	0.056912332	0.014167366	0.009549234
5.5	0.058782788	0.071153561	0.065611228	0.013081259	0.008145878
6.0	0.058538677	0.069584371	0.068031637	0.033425637	0.026237458
7.0	0.059820087	0.082310662	0.154963704	0.589915745	0.700019376
8.0	0.05889681	0.072698169	0.078609717	0.031155105	0.022300335
9.0	0.058797304	0.07140998	0.067655902	0.014604361	0.00924009
10.0	0.06024298	0.085750192	0.152106422	0.120244315	0.089621716
11.0	0.059954882	0.082938505	0.136369205	0.106353202	0.080427338
12.0	0.059760708	0.080876579	0.120132255	0.066495408	0.047760128

Table 12. 9.0 MeV MLEM

9.0 MeV					
Iteration	10	100	1000	10000	terminal (14729)
Energy (MeV)					
0.5	0.047523786	0.005180739	2.91E-06	3.17E-11	5.35E-12
1.0	0.055728279	0.015863306	0.000175905	1.45E-07	4.63E-08
1.5	0.061362443	0.031416575	0.002275079	3.12E-05	1.49E-05
2.0	0.063568075	0.04034875	0.005877594	0.000298955	0.000183523
2.5	0.0657449	0.050877896	0.0123346	0.000621303	0.000334979
3.0	0.067289966	0.05991081	0.022266555	0.002180861	0.001329676
3.5	0.067049751	0.058321858	0.019556383	0.001275057	0.000686197
4.0	0.069282536	0.073542121	0.045832942	0.006430345	0.003691566
4.5	0.070226821	0.080173615	0.054700725	0.004827616	0.002437667
5.0	0.071216982	0.088847701	0.083554623	0.013327855	0.007385887
5.5	0.072100002	0.09796047	0.141494592	0.110843569	0.091364756
6.0	0.071497423	0.091619512	0.096565791	0.018742725	0.01049626
7.0	0.072847318	0.104428783	0.150859649	0.034793521	0.019223119
8.0	0.072229003	0.099936022	0.16697314	0.19265871	0.16283158
9.0	0.072332715	0.101571841	0.197529513	0.613968116	0.700019854

Table 13. 11.0 MeV MLEM

11.0 MeV					
Iteration	10	100	1000	10000	terminal (20560)
Energy (MeV)					
0.5	0.038789645	0.003424242	2.31E-07	9.63E-16	1.47E-17
1.0	0.045564081	0.010989917	2.75E-05	5.97E-11	2.02E-12
1.5	0.050185045	0.022215822	0.000500937	4.45E-08	2.17E-09
2.0	0.051921478	0.028367044	0.001343207	6.28E-07	5.47E-08
2.5	0.053860336	0.037219117	0.00437344	1.45E-05	2.06E-06
3.0	0.055098309	0.043807141	0.008265082	5.39E-05	7.61E-06
3.5	0.054965132	0.04316853	0.008135313	7.61E-05	1.43E-05
4.0	0.056856006	0.055438962	0.024249776	0.001860199	0.000752851
4.5	0.057734641	0.061808699	0.036469781	0.003410637	0.001071436
5.0	0.058516554	0.068372832	0.05781287	0.017556039	0.010307997
5.5	0.058983053	0.072033175	0.065709616	0.013453028	0.005354558
6.0	0.058684463	0.069799832	0.062445359	0.019786071	0.010910116
7.0	0.05992308	0.08163088	0.124064694	0.094628828	0.056384823
8.0	0.059081777	0.073310549	0.074721933	0.020299049	0.008352533
9.0	0.058951061	0.071621587	0.061267263	0.006423669	0.001518664
10.0	0.060537026	0.087930178	0.168954131	0.216993699	0.146988289
11.0	0.060309134	0.086038621	0.169747664	0.504629708	0.700004393
12.0	0.06003918	0.082822872	0.131911209	0.100813869	0.058330281

$$\text{ratio} = 1 - (\text{next closest intensity/unfolded neutron}) \tag{56}$$

Ratio values for this study are listed in Table 14.

Table 14. Ratio of Unfolded Neutrons to Next Closest Neutron Intensity

Energy (MeV)	0.5	3.0	7.0	9.0	11.0
Ratio	0.9281	0.9154	0.8720	0.7674	0.7900

The ratios are the largest for lower energies because they have the most resolution between the other energies in the response functions. Higher energies are less resolved so their ratios will theoretically be the smallest, and they experience a greater effect from the probabilistic nature of Monte Carlo. In addition, due to the low resolution of high energy response functions, their responses are more difficult to unfold. These factors were evident by the next closest intensity at termination, which was not always the nearest neighboring energy bin as shown by the 7.0 MeV bin in Table 11.

The 9.0 MeV neutron in Table 12 was an exception to the standard analysis in monoenergetic unfolding. This was done to understand how the iterative process works, because this analysis did not include any neutron energies greater than 9.0 MeV. The unfolded 9.0 MeV neutron 70% termination (iteration: 14,729) came close to the unfolded 7.0 MeV neutron termination (iteration: 14,104). This means that the 9.0 MeV neutron did not have energy bins close to it with similar count values. These would have come from the 10.0 - 12.0 MeV neutrons. Unfolding according to monoenergetic neutrons is more difficult to unfold if neutron energies close to the unfolded neutron are present. This creates more 'work' for the response function to be unfolded. The 7.0 MeV neutron had more work because 6.0 and 8.0 energy neutrons were being unfolded around it. The case would have been different if greater than

9.0 MeV neutrons were considered in the unfolding of the 9.0 MeV neutron response function.

In the monoenergetic proof of the MLEM method, intensities changed depending on how many neutron energies were placed into the response function. The analysis for the 1.0 cm HDPe thickness combination used 0.5 - 12.0 MeV neutrons. The lower energies were incremented by 0.5 MeV, whereas the higher energies were incremented by 1.0 MeV because that was the smallest increment that had been measured that could successfully unfold the spectrum.

4.3 Final Solutions

The MLEM solution was obtained for both the Geant model and the experiment when all HDPe layers are 1.0 cm thick. This is plotted in Figure 34. The similarity between the model and the experiment is apparent. To quantify the difference, the ratio of the model to the experiment was tabulated in Table 15.

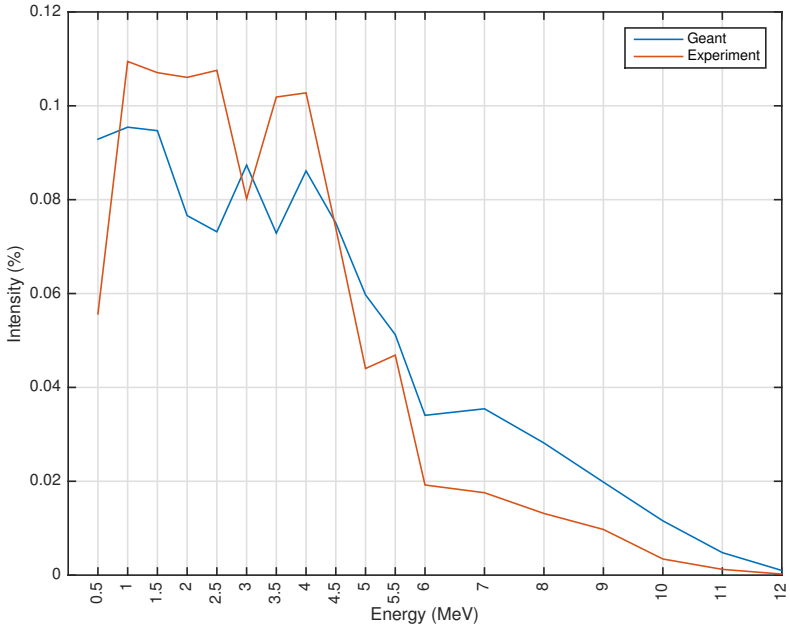

Figure 34. MLEM unfolded solution of a 1.0 cm thickness combination produced by the Geant model and the experiment.

Table 15. Ratio between Geant and the experiment.

Energy (MeV)	0.5	1.0	1.5	2.0	2.5	3.0	3.5	4.0	4.5
Ratio	1.6685	0.8721	0.8845	0.7224	0.6801	1.0893	0.7153	0.8383	1.0145

Energy (MeV)	5.0	5.5	6.0	7.0	8.0	9.0	10.0	11.0	12.0
Ratio	1.3567	1.0932	1.7729	2.0185	2.1423	2.0363	3.3631	3.9023	4.3959

The variance is a standard statistical calculation and is used to quantify the difference between the ratio and unity, where unity indicates same values between the model and experiment. The variance calculation is performed, as shown in Equation 57, and the eighteen energy groups' variances were calculated as shown in Figure 35.

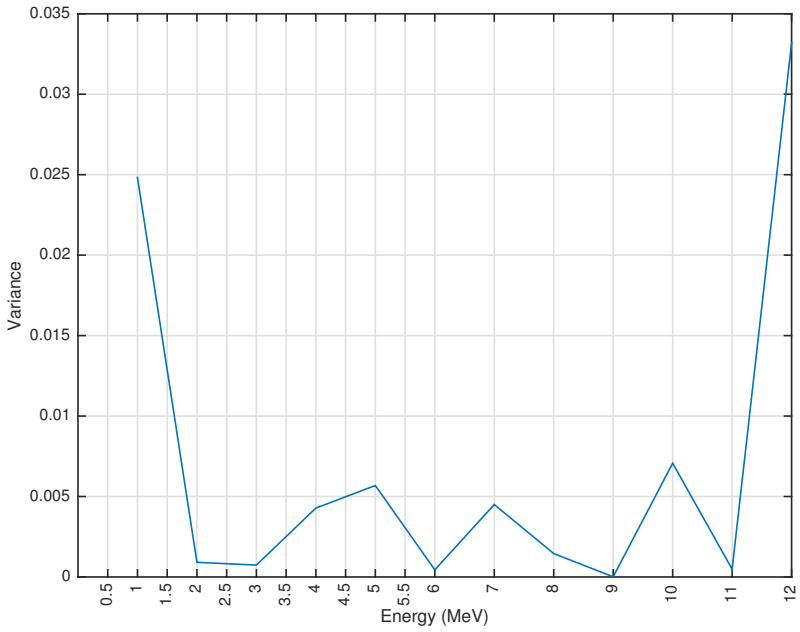

Figure 35. Variance between the difference ratio and unity between Geant and the experiment.

$$\sigma^2 = \frac{1}{N}\sum_{i=1}^{N}(x_i - \mu)^2 \tag{57}$$

Here, N is the number of energy groups, x_i is the fractional difference, and μ is unity, where there is no difference between the model and experiment. Figure 35 illustrates

that the difference between the unfolded spectra from Geant and the experiment is small, which proves that the Geant models match the experimental data well.

Reference PuBe spectra are shown in Figures 36 and 37, from Lehman et al. and Carillo et al., respectively, to compare the research results to historical data [30], [31]. They are different, as are most other PuBe reference spectra. Some appear similar but they possess variations in peak energy, peak widths, and peak intensities. These discrepancies make result comparisons difficult.

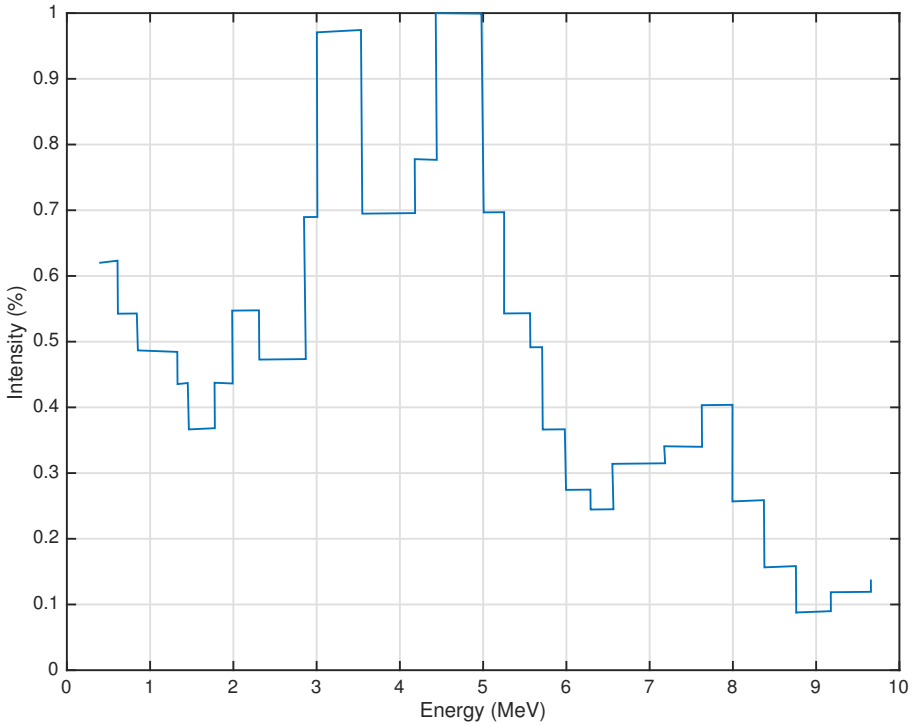

Figure 36. PuBe reference source reproduced from Lehman et al. [30].

The PuBe spectra have similarities. The most prominent peaks are around 3.5 and 5.0 MeV. The ratios of the $\sim$ 5.0 MeV peak to the $\sim$ 6.5 MeV base for the references and the $\sim$ 6.0 MeV peak to the $\sim$ 4.5 MeV base for the model and experiment are tabulated in Table 16, indicating a large variation in PuBe source spectra between reference sources. Both the model and experimental results had shifted peaks towards the lower neutron energies compared to the reference peaks from Lehman et al. and

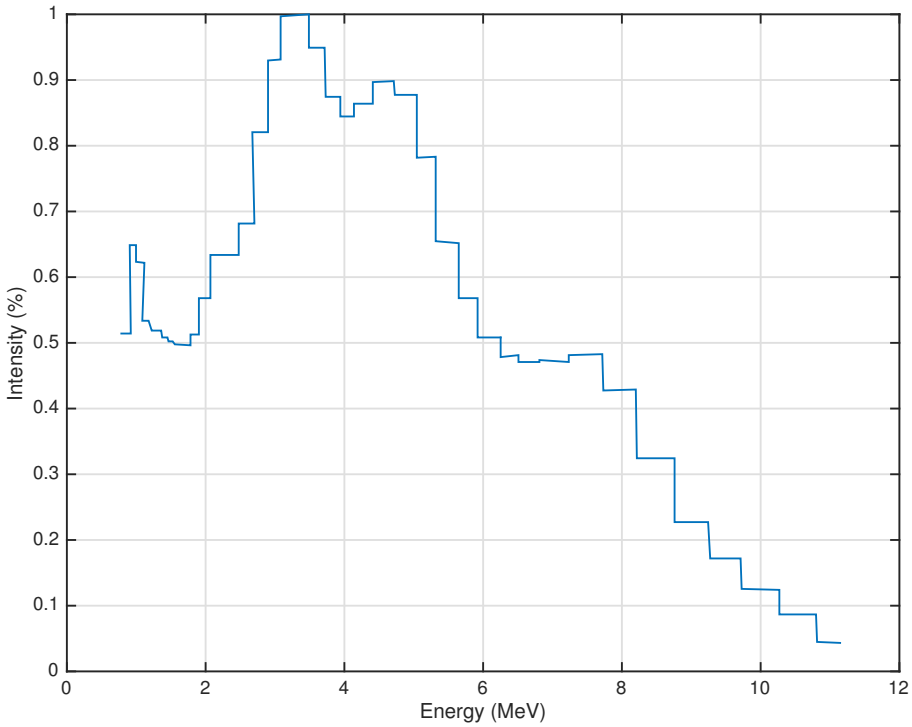

Figure 37. PuBe reference source reproduced from Carillo et al. [31].

Carillo et al. The model showed similar peak values around 3.0 and 4.0 MeV with similar full-width half-maximums; however, the experimental results showed energy peaks shifted even lower than the model, as well as broader lower energy peaks. It was speculated that the concrete walls in the experiment room may have sent lower neutron energies back to the spectrometer by creating collision events with the neutrons that were either born from the isotropic source or scattered away by the spectrometer. This would cause broader lower energy peaks in the unfolding process.

Table 16. Ratio of peak to base in reference and research spectra.

Source	Lehman	Carillo	Geant	Experiment
Peak:base ratio	4.0892	1.904	2.5324	2.3364

5. Conclusions

5.1 Summary

The purpose of this experiment was to develop a neutron spectrometer that is able to reproduce the neutron spectra from a known or unknown fast neutron energy sources, including SNM. The Geant particle transport program was used to simulate the irradiation of monoenergetic neutrons through the neutron spectrometer and develop response functions. Layers of HDPe were used to moderate the neutrons into small boron-loaded silicon diode detectors, which provided a means to unfold the spectrum.

The system was optimized using the MLEM method which was also used to unfold the fast spectrum. It is an iterative, converging, reconstructive method that takes an initial spectrum guess, response function, and source spectrum and unfolds a known or unknown source spectrum according to the response function of single unit entries (monoenergetic neutrons).

It was found that successful unfolding could be achieved using 1.0 cm layers of HDPe interleaved with the detectors, demonstrating the method for fast neutron unfolding. The 1.0 cm thick HDPe layers demonstrated that it could be unfolded correctly, and thereafter the Geant model and experiment were accurately compared. Accuracy was determined based upon statistical differences such as difference ratios and variances between the model, experiment, and reference spectra. The whole numbers were used in the model because only whole numbers were available for the experiment; matching unfolded spectra between the model and experiment was attempted with success with some similarities.

The Geant model spectrum more accurately represented the experimental spectrum than the two reference spectra. All of the spectra had similar energy peak

shapes, but the location of the energy peaks were different among the spectra. The model and experimental spectral peaks were at $\sim$ 4.5 MeV and $\sim$ 6.0 MeV, whereas the reference spectra had peaks at $\sim$ 5.0 MeV and $\sim$ 6.5 MeV. The width of the $\sim$ 4.5 MeV peak in the experiment is about 2.5 times broader than the other peaks, which may be attributed to neutron scattering in the concrete walls in the experiment room scattering and moderating neutrons. The neutrons that scatter from the wall are thermalized so they have a higher probability of detection.

5.2 Future Work

Following this research, smaller neutron energy bins at higher energies should be sampled to redefine the unfolding algorithm. This will help to identify any new requirements for detectors used in the spectrometer.

The spectrometer can be further optimized by using finer precision cuts of HDPe for the experiment and validated using the variations in HDPe thickness. The Geant optimization trials indicated an optimal thickness combination of [1.0 1.0 0.8 0.8 1.0 1.0 1.2 1.3 2.0 3.0], which could not be evaluated in this research due to a lack of fine HDPe cuts. Additional optimized configurations are given in Appendix A. The original concept for this spectrometer included cadmium layers to reduce backscattering. This method should be implemented as it will likely improve resolution at little cost in efficiency. This experiment will also have to implement cadmium layers to absorb thermal neutrons that pass through the conversion material. The response function becomes smeared if thermal neutrons are able to pass through to layers of the spectrometer to detectors behind more HDPe layers.

The Geant model boundaries were immediately outside of the spectrometer. This artificially removed neutrons reflected from external materials. The effect must be measured. The spectrometer could provide much needed neutron spectroscopy to

NREF. Analysis of the spectrometer while pulsing the source would provide a first-ever temporal neutron spectrometer measurement.

Appendix A. First Appendix

This appendix contains a library of helpful response functions. They provided insight to the development of the optimal response function.

A.1 Response Functions.

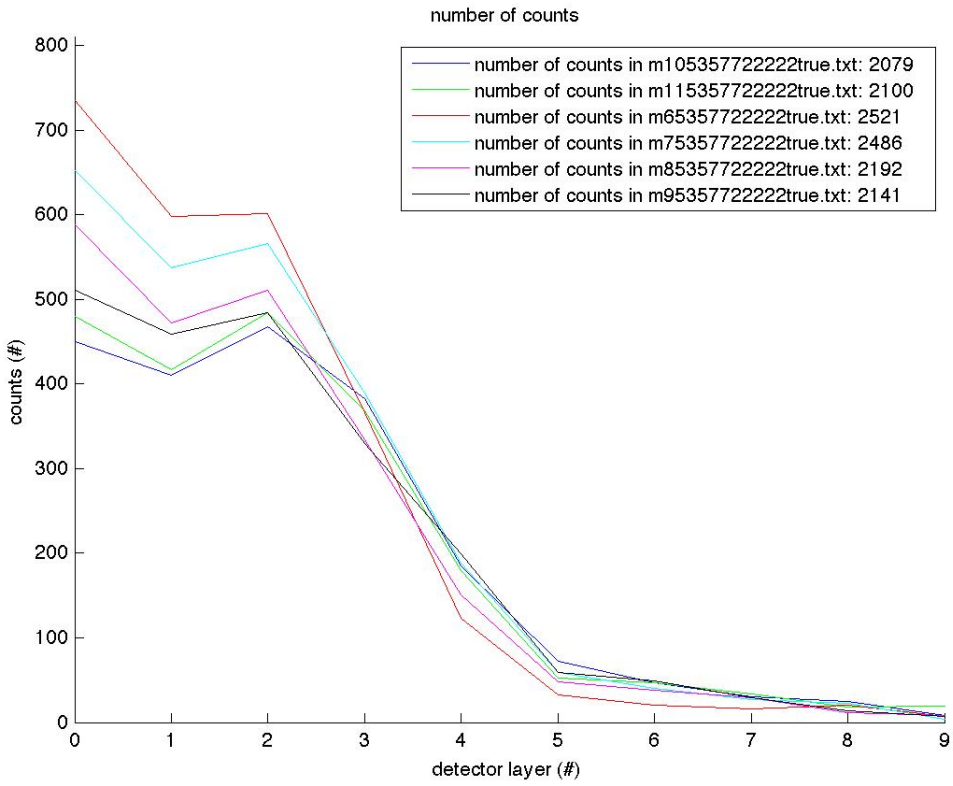

Figure 38. HDPe thickness combination [5.0, 3.0, 5.0, 7.0, 7.0, 2.0, 2.0, 2.0, 2.0, 2.0].

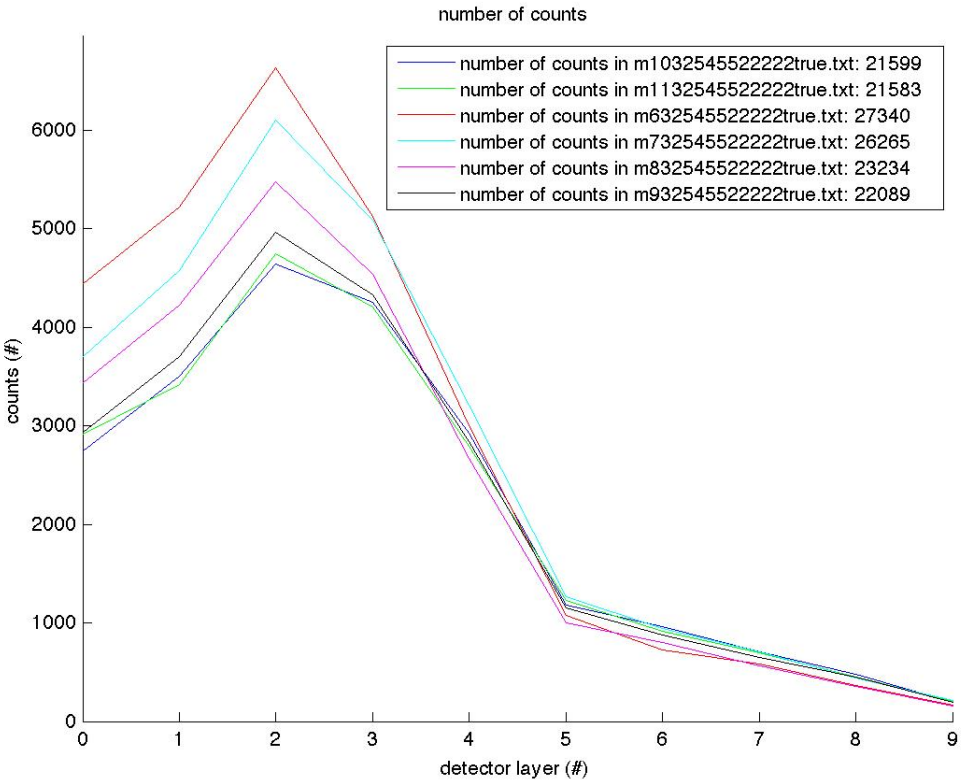

Figure 39. HDPe thickness combination [3.0, 2.0, 5.0, 4.0, 5.5, 2.0, 2.0, 2.0, 2.0, 2.0].

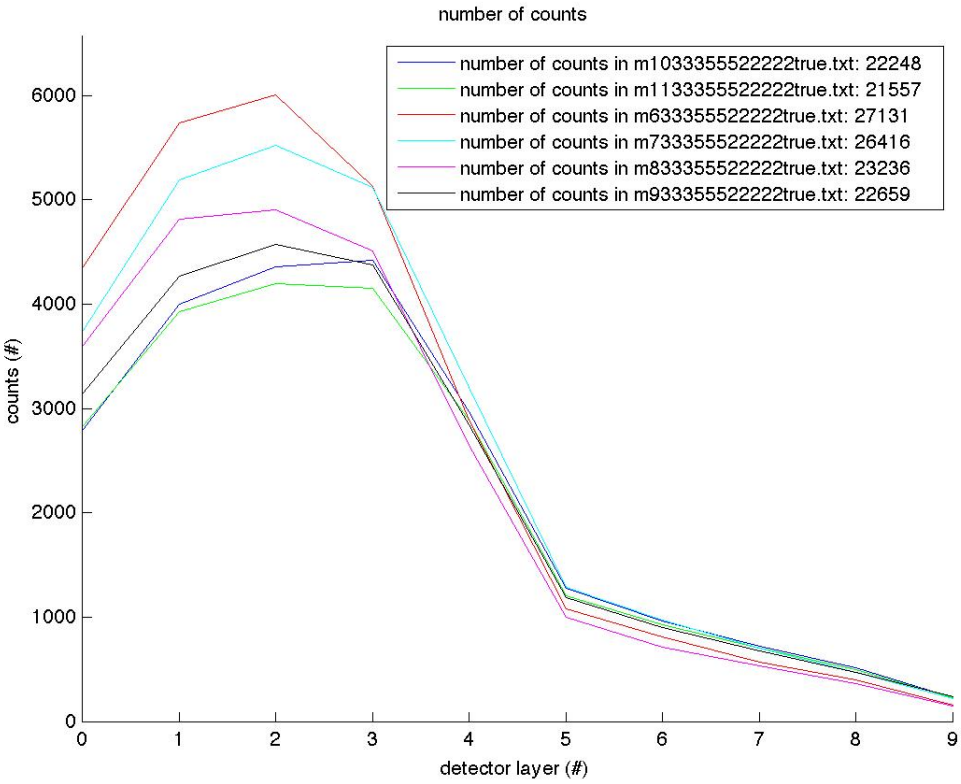

Figure 40. HDPe thickness combination [3.0, 3.0, 3.5, 5.0, 5.0, 2.0, 2.0, 2.0, 2.0, 2.0].

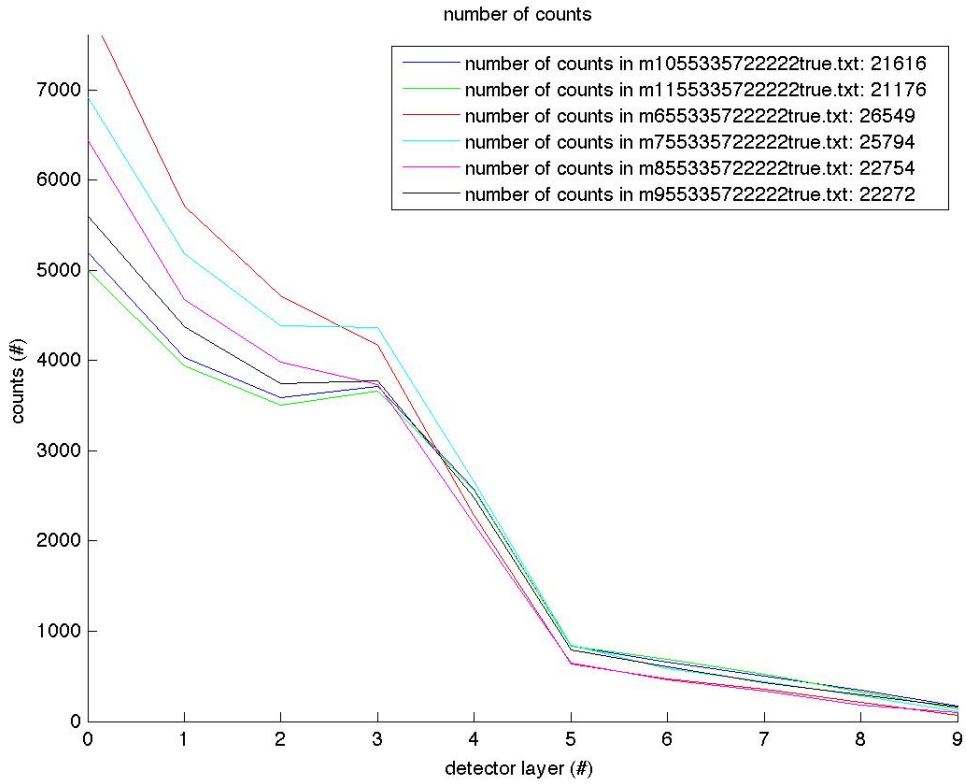

Figure 41. HDPe thickness combination [5.5, 4.0, 4.0, 5.0, 7.0, 2.0, 2.0, 2.0, 2.0, 2.0].

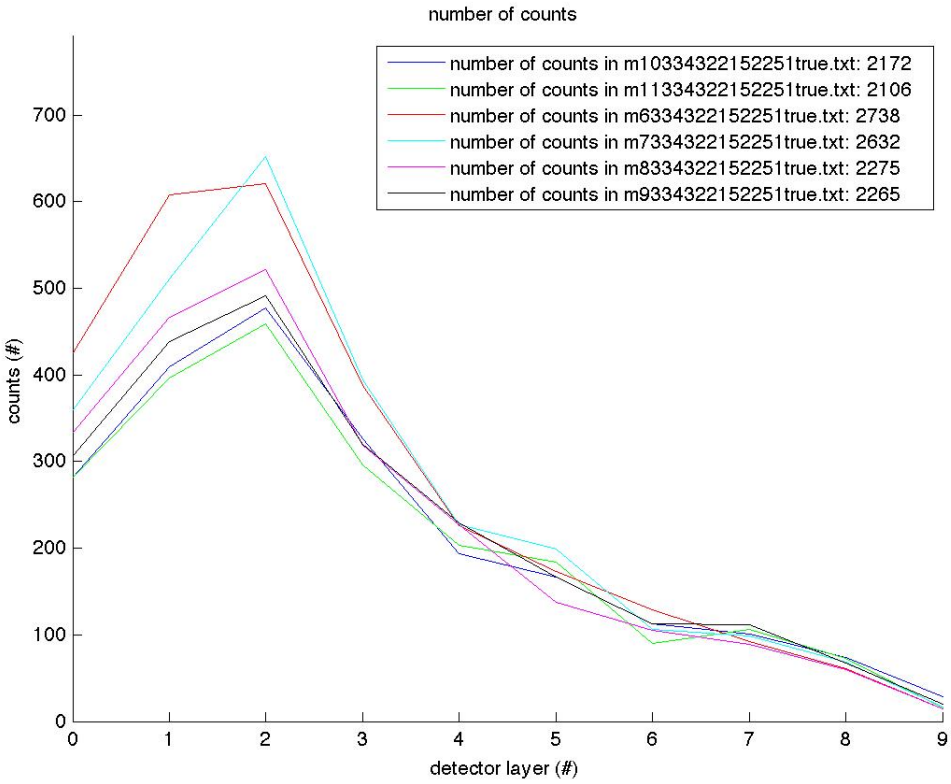

Figure 42. HDPe thickness combination [3.3, 4.0, 3.0, 2.0, 2.0, 1.5, 2.0, 2.0, 5.0, 1.0].

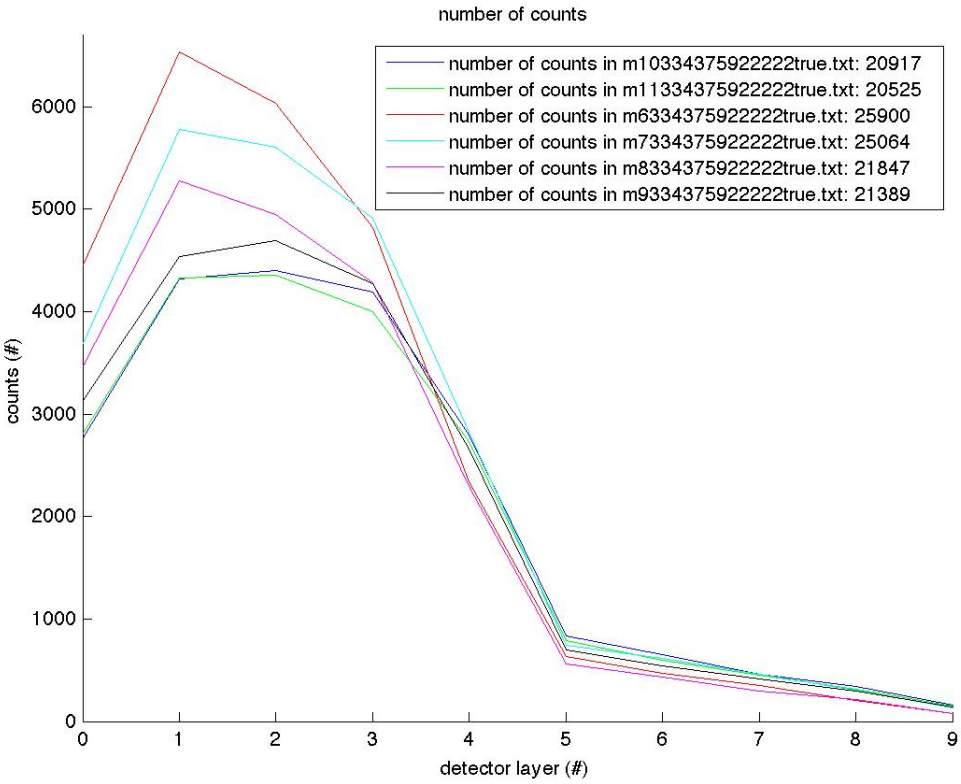

Figure 43. HDPe thickness combination [3.3, 4.0, 3.0, 7.5, 9.0, 2.0, 2.0, 2.0, 2.0, 2.0].

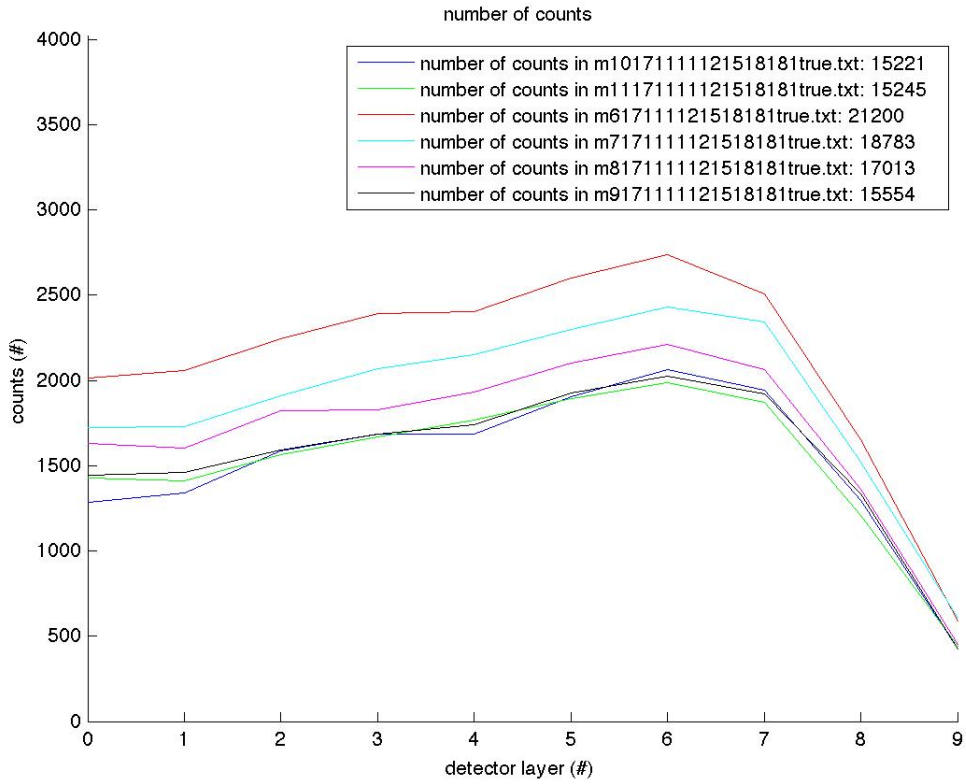

Figure 44. HDPe thickness combination [1.7, 1.0, 1.0, 1.0, 1.0, 1.2, 1.5, 1.8, 1.8, 1.0].

Bibliography

1. "Nuclear Test Ban Treaty," http://www.jfklibrary.org/JFK/JFK-in-History/Nuclear-Test-Ban-Treaty.aspx, accessed: 2016-01-09.

2. J. Bevins *et al.*, "Targeted Modification of Neutron Energy Spectra for National Security Applications," unpublished.

3. M. Halstead *et al.*, "Investigating Time and Spectra Dependence in Neutron Radiation Environments for Semiconductor Damage Studies," Ph.D. dissertation, Air Force Institute of Technology, 2014.

4. T. Oakes *et al.*, "An Accurate and Portable Solid State Neutron Rem Meter," *Elsevier Inc.*, 2013.

5. J. Coderre, "Principles of Radiation Interactions: Neutrons," Massachusetts Institute of Technology Lecture, 2004.

6. J. Clinton *et al.*, "Optimization and Characterization of a Novel Self Powered Solid State Neutron Detector," Ph.D. dissertation, Air Force Institute of Technology, 2011.

7. G. F. Knoll, *Radiation Detection and Measurement, 4th ed.* New York: Wiley, 1979.

8. "Evaluated Nuclear Data File," http://www.nndc.bnl.gov/exfor/endf00.jsp, 2016, accessed: 2016-01-09.

9. "Solving for Depletion Region," http://www.pveducation.org/pvcdrom/pn-junction/solving-for-depletion-region, 2016, accessed: 2016-01-09.

10. "Principles of Semiconductor Devices: Chapter 4: p-n Junctions," http://ecee.colorado.edu/~bart/book/book/chapter4/ch4_5.htm, 2011, accessed: 2016-01-09.

11. J. J. Duderstadt and L. J. Hamilton, *Nuclear Reactor Analysis.* New York: Wiley, 1976.

12. "A Few Good Moderators: The Numbers," http://energyfromthorium.com/2007/02/13/a-few-good-moderators-the-numbers/, accessed: 2016-01-09.

13. P. Rinard, *Neutron Interactions with Matter.* Office of Nuclear Regulatory Research, 2007.

14. M. N. Wernick and J. N. Aarsvold, *Emission Tomography: The Fundamentals of PET and SPECT.* Amsterdam: Elsevier Inc., 2004.

15. A. Dempster *et al.*, "Maximum Likelihood from Incomplete Data via the EM Algorithm," *Journal of the Royal Statistical Society*, 1977.

16. "What is the Monte Carlo Method?" http://www.goldsim.com/Web/Introduction/Probabilistic/MonteCarlo/, accessed: 2016-01-09.

17. P. Saidi, P. Sadeghi, and C. Tenreiro, *Theory and Applications of Monte Carlo Simulations*. InTech, 2013.

18. S. Agostinelli *et al.*, "Geant4 - A Simulation Toolkit," *Elsevier Inc.*, 2003.

19. M. Pia, "The Geant4 Object Oriented Simulation Toolkit."

20. "Geant4: Planned Developments for 2015," http://geant4.cern.ch/support/planned_features.shtml, accessed: 2016-01-09.

21. M. Ford *et al.*, "Neutron Spectrometer Using LiF Thin Film Detector," Master's thesis, Air Force Institute of Technology, 2013.

22. H. Vega-Carrillo *et al.*, "Characterization of a 239PuBe Isotopic Neutron Source," *Proceedings of the ISSSD*, 2012.

23. Z. Harvey, "Neutron flux and energy characterization of a plutonium-beryllium isotopic neutron source by Monte Carlo simulation with verification by neutron activation analysis," *University Libraries, University of Nevada, Las Vegas*, 2010.

24. J. Cvachovec and F. Cvachovec, "Maximum Likelihood Estimation of a Neutron Spectrum and Associated Uncertainties," *AiMT*, 2008.

25. *Ortec: GammaVision: Software User's Manual*, Ametek.

26. D. Pengra, "The Oscilloscope and the Function Generator," 2007.

27. *Ortec: GammaVision 8, Gamma Spectroscopy Software*, Ametek.

28. *Ortec: GammaVision: Software User's Manual*, Ametek.

29. K. Okuno, "Application of neutron shield concrete to neutron scattering instrument TAIKAN in J-PARC," *Progress in Nuclear Science and Technology*, 2014.

30. R. Lehman, "The Origin of Neutron Groups in Be(α, n) Sources." *Elsevier Inc.*, 1967.

31. H. Vega-Carillo and C. Torres-Muhech, "Low Energy Neutrons from a ^{239}PuBe Isotopic Neutron Source Inserted in Moderating Media." *Investigación*, 2002.

REPORT DOCUMENTATION PAGE

Form Approved
OMB No. 0704–0188

The public reporting burden for this collection of information is estimated to average 1 hour per response, including the time for reviewing instructions, searching existing data sources, gathering and maintaining the data needed, and completing and reviewing the collection of information. Send comments regarding this burden estimate or any other aspect of this collection of information, including suggestions for reducing this burden to Department of Defense, Washington Headquarters Services, Directorate for Information Operations and Reports (0704–0188), 1215 Jefferson Davis Highway, Suite 1204, Arlington, VA 22202–4302. Respondents should be aware that notwithstanding any other provision of law, no person shall be subject to any penalty for failing to comply with a collection of information if it does not display a currently valid OMB control number. **PLEASE DO NOT RETURN YOUR FORM TO THE ABOVE ADDRESS.**

1. REPORT DATE *(DD–MM–YYYY)*	2. REPORT TYPE	3. DATES COVERED *(From — To)*
24–03–2016	Master's Thesis	June 2014 - March 2016

4. TITLE AND SUBTITLE

Neutron Spectroscopy Optimization Using a Solid State Thermal Neutron Detector

5a. CONTRACT NUMBER

5b. GRANT NUMBER

5c. PROGRAM ELEMENT NUMBER

6. AUTHOR(S)

Eichert, Carl J., 2d Lt, USAF

5d. PROJECT NUMBER

JON16P188

5e. TASK NUMBER

5f. WORK UNIT NUMBER

7. PERFORMING ORGANIZATION NAME(S) AND ADDRESS(ES)

Air Force Institute of Technology
Graduate School of Engineering and Management (AFIT/EN)
2950 Hobson Way
WPAFB OH 45433-7765

8. PERFORMING ORGANIZATION REPORT NUMBER

AFIT-ENP-MS-16-M-066

9. SPONSORING / MONITORING AGENCY NAME(S) AND ADDRESS(ES)

Domestic Nuclear Detection Agency
POC: Samantha Connelly
245 Murray Ln SW #0115
Washington DC 20528
samantha.connelly@dhs.gov

10. SPONSOR/MONITOR'S ACRONYM(S)

DNDO

11. SPONSOR/MONITOR'S REPORT NUMBER(S)

12. DISTRIBUTION / AVAILABILITY STATEMENT

Distribution Statement A. Approved for public release; Distribution Unlimited.

13. SUPPLEMENTARY NOTES

This material is declared work of the U.S. Government and is not subject to copyright protection in the United States.

14. ABSTRACT

AFIT is researching methods for radiation detection that allow for fast analysis of neutron spectra for energies up to 14 MeV. The initial research includes the design and analysis of a neutron spectrometer using high-efficiency solid state detectors separated by multiple layers of high density polyethylene and cadmium. The spectrometer design was modeled and optimized computationally using GEANT4.10.1; a range of monoenergetic neutron sources were modeled, resulting in a theoretical response function matrix for several different polyethylene layer thicknesses. These response functions and source spectra from historical experimental data and spectra can then be used in a Maximum-Likelihood Expectation-Maximization unfolding routine to unfold the spectra of polyenergetic sources. The key to the success of this research is obtaining the resolution needed between the detectors to unfold the spectrum, while making the system of thermalizing polyethylene layers and detectors as efficient as possible. This presentation will discuss the process used to develop the algorithm and models and determine efficiency, including experiments to validate the results.

15. SUBJECT TERMS

neutron, spectroscopy, moderation, detection, MLEM, unfold

16. SECURITY CLASSIFICATION OF:			17. LIMITATION OF ABSTRACT	18. NUMBER OF PAGES	19a. NAME OF RESPONSIBLE PERSON
a. REPORT	b. ABSTRACT	c. THIS PAGE			Dr. James C. Petrosky, AFIT/ENP
U	U	U	UU	106	19b. TELEPHONE NUMBER *(include area code)* (937)255-3636 x.4562; james.petrosky@afit.edu